STUDY OF THE TRAJECTORIES OF ICE SHED BY DEICING SYSTEM AROUND AIRCRAFT ENGINE

by

Hassan EL SAHELY

THESIS PRESENTED TO ÉCOLE DE TECHNOLOGIE SUPÉRIEURE IN PARTIAL FULFILLMENT FOR A MASTER’S DEGREE WITH THESIS IN ENGINEERING CONCENTRATION AEROSPACE
M.A.Sc

MONTREAL, DECEMBER 12, 2019

ÉCOLE DE TECHNOLOGIE SUPÉRIEURE
UNIVERSITÉ DU QUÉBEC

BOARD OF EXAMINERS

THIS THESIS HAS BEEN EVALUATED

BY THE FOLLOWING BOARD OF EXAMINERS

Mr. François Morency, Thesis Supervisor
Department of Mechanical Engineering, at École de Technologie Supérieure

Mr. Stéphane Hallé, President of the Board of Examiners
Department of Mechanical Engineering, at École de Technologie Supérieure

Mme Marlène Sanjosé, Member of the jury
Department of Mechanical Engineering, at École de Technologie Supérieure

THIS THESIS WAS PRESENTED AND DEFENDED

IN THE PRESENCE OF A BOARD OF EXAMINERS AND PUBLIC

ON DECEMBER 03, 2019

AT ÉCOLE DE TECHNOLOGIE SUPÉRIEURE

ACKNOWLEDGMENT

This thesis is done through two years in which professor Francois Morency played an essential role in supervising and advising me to the correct path by his intelligent ideas. I am grateful and thankful to him. I would like to thank all the members of TFT laboratory for their continuous support specially Abdallah, Olivero, Kevin, Sami, Sébastien, Violaine, Gitsuzo and Ahmed. I would like to tell them that your effort is highly appreciated.

I would like to thank god in the first place for giving me the power and strength to achieve this work. Also, my small family was supportive emotionally and financially and without them it’s impossible to achieve what I am now. I want to tell my parents it’s time to be proud of your son.

Étude des trajectoires des particules de glace par système de dégivrage autour du moteur de l'avion

Hassan EL SAHELY

RÉSUMÉ

Le problème de l'accumulation de glace a causé des accidents et des incidents aux aéronefs au cours des dernières décennies. La résolution du problème de l'accumulation de glace à l'aide de dispositifs de dégivrage et d'antigivrage permettra d'éliminer la glace accumulée, mais le problème des trajectoires inconnues des particules détachées apparaît. Les particules de glace représentent un grand danger pour l'aéronef. Le risque varie en fonction de la vulnérabilité des pièces de l'aéronef. Les parties vulnérables de l'avion sont l'aile, le fuselage arrière, les stabilisateurs et les moteurs montés à l'arrière. Afin d'atténuer le risque, une étude des trajectoires des particules est introduite. L'objectif de cette recherche est d'étudier les trajectoires autour d'une aile en changeant l'angle d'attaque et l'angle de flèche. Le but est de calculer le nombre minimal de trajectoires de glace pour prédire correctement une carte d'empreinte à la section d'entrée du moteur en utilisant la méthode de Monte-Carlo. Une approche numérique est utilisée pour réaliser cette étude. Les trajectoires aléatoires des particules de glace sont calculées à l'aide d'un champ de vitesse calculé par la méthode des panneaux 3D (3DPM). Pour déterminer les zones derrière l'aile où les particules de glace ont la plus grande probabilité de passage, une méthode de Monte-Carlo est utilisée. Dans cette recherche, les calculs sont effectués au moyen d'une étude probabiliste des empreintes pour déterminer la forme de leur distribution de probabilité. Une fois la forme connue, un test de normalité est effectué sur la forme de la fonction de distribution de probabilité (PDF) appelé le test Kolmogorov-Smirnov. Après avoir déterminé la forme et le type des PDF, une étude sur la moyenne et la variance pour chaque PDF est effectuée pour vérifier le nombre minimal de trajectoires nécessaire pour la méthode de Monte-Carlo. Le champ d'écoulement de 3DPM est validé par rapport à la littérature ainsi qu'à la répartition de l'empreinte derrière l'aile. L'effet de l'angle d'attaque, ainsi que l'angle de flèche sur les trajectoires de particules de glace, est montré. L'augmentation de l'angle d'attaque déplace les trajectoires vers le haut tandis que la flèche rend la carte d'empreinte moins bruitée. Enfin, 500 trajectoires sont suffisantes pour prévoir une carte d'empreinte.

Mots-clés: Accumulation de glace, PDF, carte d'empreinte, méthode de Monte-Carlo.

Study of the trajectories of ice shed by deicing system around aircraft engine

Hassan EL SAHELY

ABSTRACT

The problem of ice accretion caused accidents and incidents to aircraft over the past decades. Solving the problem of ice accretion employing de-icing and anti-icing devices will remove the accumulated ice but the problem of unknown trajectories of the detached particles appears. The flown particles represent a great hazard on the aircraft which yields risk depending on the vulnerability of aircraft parts. The vulnerable aircraft parts are the wing, the rear fuselage, the stabilizers, and the rear-mounted engines. In order to mitigate the risk, a study of the trajectories of those particles is introduced. The objective of this research is to study the trajectories around a wing by changing the angle of attack and the sweepback angle. The goal is to calculate the minimal number of ice trajectories to correctly predict a footprint map at the inlet section of the engine using the Monte-Carlo method. A numerical approach is used to accomplish this study. The random trajectories of the ice particles are calculated using a 3D Panel Method (3DPM) flow field around the wing. To determine the zones behind the wing where the ice particles have the most passage probability, a Monte-Carlo method is utilized. In this research, the calculations are done through a probabilistic study of the footprints to determine their probability distribution's shape. Once the shape is known, a normality test is done on the shape of the Probability Distribution Function (PDF) called the Kolmogorov-Smirnov test. After determining the shape and the type of the PDFs, a study on the mean and variance for every PDF is done to check the minimal number of trajectories to fulfill the Monte-Carlo method. The 3DPM flow field is validated against the literature as well as the footprint distribution behind the wing. The effect of the angle of attack, as well as the sweepback angle on ice particle trajectories, is shown. The increase of the angle of attack shifts the trajectories upward while the sweepback makes the footprint map less noisy. Finally, 500 trajectories were found enough to predict a footprint map.

Keywords: Ice accretion, PDF, footprint map, Monte-Carlo method.

TABLE OF CONTENTS

Page

LIST OF TABLES

LIST OF FIGURES

Page

LIST OF ABREVIATIONS

CFD	Computation fluid Dynamics
BWB	Blended Wing Body
3DPM	3D Panel Method
GA	Ground Aviation
CFR	Code Federal Regulation
2D	Two dimensional
3D	Three-dimensional
FAA	Federal Aviation Administration
NASA	National Aviation and Space Administration
PDF	Probability Distribution Function
TFT	Laboratory of ThermoFluide pour le Transport
AR	Aspect ratio
DOF	Degree of freedom
CP	Centre of pressure
CG	Center of gravity
MATLAB	Matrix Laboratory
SR	Surface Ratio
SBA	Sweepback angle
AOA	Angle Of Attack
AOPA	Aircraft Owners and Pilots Association
NTSB	National Transportation and Safety Board

LIST OF SYMBOLS

Φ	Potential flow velocity
σ	Source strength
μ	Doublet strength
ζ	The skid angle
c	Chord
I	Inertial matrix of the flat plate
P, Q, R	Angular velocity of the debris particle in the three axis of rotation
m	Mass of the particle
V_{re}	Relative velocity
α	Angle of attack
β	Side slip angle
F_{np}	Normal resultant force on the particle
D	Drag force
L	Lift force
L, l, e	Length, width and thickness of the particle
g	Gravitational force
C_{dm}	Coefficient of dynamic moment
C_N	Normal resultant force coefficient
N	Total number of trajectories
h	Bandwidth coefficient
Up, Vp, Wp	Velocity components of the particle in the global frame of reference
u_s, v_s, w_s	Velocity components of the particle due to source
u_d, v_d, w_d	Velocity components of the particle due to doublet
ε	Error
q_1, q_2, q_3, q_4	Quaternions
Ω	Vector rotation of the flat plate
X_c, Y_c, Z_c	Coordinates of the collocation point
ρ	Density

INTRODUCTION

The problem of icing on wings is a serious problem in aviation. The ice accretion on the wing's leading edge increases the drag and disturbs the smooth air around the wing, thus destroying lift creation (FAA,2008). Flying in such conditions will cause hazards for the aircraft, leading to emergency descent or crash. The problem of ice accretion on wings has caused many incidents and accidents recorded over the past three decades. For example, the Embraer EMB-500 Phenom 100 on December 8, 2014, crashed because of the ice accretion on the wing caused the aerodynamic stall (NTSB,2016). Figure 0.1 shows an illustration of an aircraft with an iced wing (Bremmer,2018). It demonstrates the perturbation of the flow around the lifting surface. This flow perturbation is shown in the picture by the streamlines in blue color.

Figure 0.1 Inflight icing on the non-protected surfaces (Bremmer, 2018)

12 % of the total crashes related to weather conditions according to 10 years statistics between 1990 and 2000, were linked to icing (AOPA,2008). Moreover, in the four years between 2010 and 2014, the National Safety Transportation statistics reported many major accidents. The 52 recorded accidents led to 78 fatalities (AOPA,2008). To avoid these types of incidents and accidents, ice accumulation could be eliminated in two ways: either by deicing systems or with

anti-icing systems. Deicing removes the ice accretion after being accumulated, but anti-icing prevents any ice accretion on the aircraft surfaces. One of the solutions suggested to remove the ice accumulated inflight is a flexible membrane on the leading edge called a “Flexible rubber boot” (FAA,2008). This membrane expands and contracts, to remove the accumulated ice on the leading edge (FAA,2008).

The ice accreted on the leading edge is detached employing de-icing devices. Some particles will hit the aircraft and the majority will fly downstream the flow. While flying, the ice particles detached from the wing leading edge will transform into a flying hazard. It can cause damage to the aircraft parts such as the fuselage, stabilizers or the rear mounted engines. The manufacturers take into consideration the hazard of flying ice particles in order to minimize their probability of being ingested by the engines (Suares,2005). If the ice particles strike the engine, serious damage will occur to the fan blades and other engine parts (Morse,2004).

The goal of this work is to build a tool that enables quick study of the wing geometry on footprint maps. In this study, a numerical method is used to simulate the trajectories of the ice particles. The method used to obtain the flow field around the wing is a 3D based panel method (3DPM), that uses source and dipole singularities. Previous studies used 3D computational fluid dynamics (CFD) and computational domain around a geometry to calculate the velocity flow field in the near and farfield such as (Papadakis et al, 2007), (Ignatowicz et al., 2019), (Deschenes, Baruzzi, Lagace, & Habashi, 2011), (Suares,2005). All these studies used a CFD mesh to discretize the volume around the aircraft. The CFD method calculates the three components of the fluid velocity at all nodes of the mesh. The trajectory is calculated based on Newton’s second law of motion by interpolating velocity from the computed CFD solution at each node. One of CFD negatives is the difficulties of mesh generation which requires skills and time. After generating the mesh depending on its size, the flow solution should be generated as well. When the mesh is finer, then the interpolation between the nodes to find the velocity will require even more time. But in 3DPM the solution is generated quickly. The 3DPM asks only for the airfoil coordinates then the surface mesh is directly generated.

The trajectories can cross a certain plane after the wing, perpendicular to the fuselage (it will be specified in the methodology section). At this specific plane, the footprints of the trajectories will be collected. The collected footprints form an icing footprint map. To well predict the footprint map of the ice particles, a Monte-Carlo method should be used (Papadakis et al., 2007). To perform this approach a huge number of trajectories should be simulated. The main challenge facing the Monte-Carlo method is the computation time for the trajectory's calculation. The objective of this research is to perform a Monte-Carlo approach with a reduced number of trajectories by assuming a specific shape of the probability distribution function (PDF) of the footprints at the plan of interest. The proposed method only needs a surface mesh of the solid body to compute the flow field. The 3D Panel Methods ables to computes the velocity at all points on the surface of the solid body (wing) and in the farfield. The calculation of the trajectories is based on the Newton's second law of motion in the Lagrangian frame of motion. Moreover, for the calculation of the resultant aerodynamic force, the aerodynamic coefficient must first be calculated, taking into account local angle of attack and side slip angle of the particle through correlations, instead of calculating all aerodynamic forces at each time. A 3D dynamic moment and static moment are also applied to the particle (rectangular flat plate in this case) since the particle rotates while moving. The PDF should be evaluated based on the footprint map data. Thus, the data are fitted in a fitter app to check their PDF shape. For every number of trajectories simulated, a shape of the correspondent PDF is obtained and tested. The shape of the functions is then compared. After that, a study of the PDF characteristics is done to show the optimal number of trajectories needed to fulfill Monte-Carlo approach by changing the angle of attack and the sweepback angle.

This thesis is divided into three chapters. In the first chapter, a review of literature is conducted to reveal the state of the art of this research with respect to previous researches in the same domain. The first chapter starts considering the inflight icing conditions and how flying in such conditions could adversely affect the aircraft. In addition, computations of the ice trajectories using CFD and 3DPM flow field from the literature are illustrated. Moreover, trajectories simulation techniques are exposed. Finally, an illustration of the Monte-Carlo approach used for ice-particle simulations is carried out.

Chapter two will present the methodology of this research. The equations used in the mathematical model are implemented into a MATLAB code to compute the trajectories in a non-uniform flow field. Also, in this chapter, an algorithm is proposed to close the wingtip of the grid used in order to correct the flow field around the wing. Finally, the Monte-Carlo approach with an assumed probability distribution function is presented.

Chapter three will present the results of this study. A validation of the flow field is done against the experimental data. A comparison with the literature reveals a verification of the proposed methodology as well as a validation with Suares (2005). A Monte-Carlo study is done to compute the probability distribution of the trajectories at a plan downstream of a wing. The effect of the angle of attack will be investigated as well as the sweepback angle. Finally, A probabilistic study will be performed to check the correct number of trajectories computation needed to fulfill the Monte-Carlo study.

CHAPTER 1

REVIEW OF LITERATURE

This section presents a review of the studies done in the literature related to the domain of aircraft de-icing. This review is classified into four sub-sections: Flying in icing conditions, ice particle shedding simulation, ice shed computation method and Monte-Carlo simulation on trajectories.

1.1 Flying in icing conditions

During flight, especially where the temperature is near the freezing point and below, ice may accrete on the non-protected surfaces of the aircraft and may lead to degradation of the wing performance (Cebeci & Besnard, 1994). The saturated clouds form a layer of ice on the surface of the wing's leading edge, nose and fin. There are many numerical and experimental models for ice formation presented in the literature (horn ice, rime ice, glaze ice), (Cao, Zhang, & Sheridan, 2019), (Papadakis, Yeong, Wong, Vargas, & Potapczuk, 2005). The ice formed could be de-iced locally on the aircraft parts by different methods: mechanically, either by using a flexible membrane which inflates or mechanical actuators (Venna & Lin, 2006), and electrically by applying an electric current to heat up the surface and detach the buildup ice (Giamati, Leffel, & Wilson, 1995). Others like Petrenko (2010), used a combination of an electrothermal and electromechanical deicing system. The detachment of the ice will solve the problem of wing reshape to gain back its performance, but it results on appearance of another problem, which is the random trajectories of those particles. The detached particles have random shapes volumes and masses, and may strike the aircraft parts like windows or rear-mounted engine (Mason, Strapp, & Chow, 2006) that lead to fatal consequences.

Petty et Floyd (2004) presented a statistical study on aircraft icing accidents. The accidents due to ice accumulation on the airframe are grouped into three categories: GA (General Aviation), 14 CFR (Code Federal Regulation) Part 135 and Part 121. Petty et Floyd mentioned that 583 accidents were recorded between 1982-2000. The accidents lead to 819 fatalities according to

National Transportation and Safety Board (NTSB) in Washington DC. The NTSB's study also showed that the percentage of aircraft accidents, due to icing, depends on the flight phase. The study deduced that the highest accident percentage was found in the cruising flight phase.

To study and test ice accumulation on aircraft parts is not an easy task. To check how the aerodynamic forces on the aircraft changes, experimental tests should be done. Figure 1.1 shows the ice particle detachment from the wing leading edge. This experiment was done by NASA. It shows clearly how the trajectories of the ice pieces possess different shapes. The trajectories of the ice particles goes the same direction as the flow.


Source: NASA Ames Imaging Library Server

Figure 1.1 Ice particles detaching from the wing leading edge experimentally by NASA using electro-expulsive system.

Aircraft manufacturers and aviation authorities try to predict the problem of ice accretion for risk mitigation. This aspect is expensive and cost the aircraft manufacturer a lot. In fact, tests in wind tunnel, for example like the experiments done by Papadakis et al., (2007), under specific icing conditions could be less expensive than doing the same test inflight. Going toward computer simulations may be a good solution as well to minimize the study costs. These simulations could give results with excellent agreement with the experimental data if they are well performed.

1.2 Ice-particle trajectory simulation

Some researchers have modelled the ice shedding problems and proposed ways to estimate the danger in some regions downstream of the main aircraft parts. This section highlights the most relevant previous studies about ice shedding.

One of the first researches in the panel method for 2D and 3D meshes was done by Hess et Smith (1967) for Douglas company. This method was revolutionary at that time because it was able to predict correctly the flow field around an arbitrary body. Later, Katz et Plotkin (2001) explained also the panel method for 2D and 3D based on Hess and Smith. NASA in 1991 published research about developing the PMARC program which was based on the 3D panel method (Ashby, Dudley, Iguchi, Browne, & Katz, 1991). These methods compute the flow field around the solid body and enable the calculation of the flow field parameters for trajectories calculation.

Kohlman et Winn (2001) studied the ice pieces trajectories of a particle with 4-DOF (three translational and pitching angle) in a uniform flow field. The ice-piece is a square with a uniform thickness shed from the fuselage. The initial angle of attack, the damping coefficient and the thickness of the plate were predefined as initial conditions. The main model is based on the Newton’s second law of motion. Aerodynamic forces (lift and drag) on the square are calculated from aerodynamic coefficients. The aerodynamic coefficients are calculated using correlations that depend on the angle of attack and the rotation velocity. A sensitivity study was conducted to determine the effect of the size and the thickness of the shed ice shapes. The results show that the ice piece rotation depends on the damping coefficient and the angle of attack. Also, the trajectory position is obtained by varying the following parameters: the size of the ice-piece, the damping coefficient, the thickness of the particle and the angle of attack.

Santos, Papa, et Do Areal Ferrari (2003) simulated ice trajectories based on CFD solution from FLUENT. The trajectory calculation is based on correlations for aerodynamic coefficients obtained from the literature. The whole methodology was based on the one proposed by Kohlman et Winn (2001). The study was limited to a number of parameters: the angular velocity, the initial angle of rotation, and the pitch damping coefficient. The ice shedding was from a fixed location x = -0.1 m, y = 0.1 m and z = 0.1 m. The results show the probability distribution at the plane x = 8 m after the wing in a 0.5 m discretization along the z-axis. They used a low number of trajectories of 343. The addition of Santos to Kohlman's work is that the methodology of Santos was combined with CFD flow field results in order to evaluate the risk of impact of the ice pieces at specified areas in a cross-section plan downstream the flow.

The windborne debris trajectories has been studies in the field where the impact of hurricanes should be studied. Holmes, Letchford, et Lin (2006) conducted a 2D simulation of the debris trajectories. Their study was done numerically and experimentally in the wind tunnel at Texas Tech University. They used only a square plate as a representation of the debris but with various dimensions. The calculations of the lift, drag and moments applied to the debris were calculated based on aerodynamic coefficients, which are function of the angle of attack. The trajectory of the debris was calculated by means of the Newton's second law of motion in a uniform flow field. Holmes compared the results with the results obtained by Tachikawa (1983). The results show a comparison of the trajectories with and without Magnus effect. The Magnus effect is the rotation of the particle caused by the fluid motion which creates additional lift force. This additional lift force could be positive or negative depending on the initial angle of rotation the debris. The normal force coefficient, the center of pressure position, and the Magnus effect lift showed their importance for trajectories computations.

Kordi et Kopp (2009) used Newton's second law of motion to predict trajectories of flat plates in a uniform flow field. The model is based on dimensionless initial parameters: rotational lift, drag, pitching moment and velocity. The Magnus effect was considered. The autorotation of the plate was taken into account as a single degree of freedom system experimentally to estimate onset of the autorotation, the tip speed and the coefficient of the forces. The results were compared to the experimental results obtained by Tachikawa (1983). The aspect of this study focused on the asymptotic limits of the dimensionless rotational, vertical and horizontal speeds as function of the geometry as well as the aerodynamic forces. Kordi and Kopp noticed that the dimensionless parameters governing the trajectories of the debris are the angular velocity, the pitching angle, the rolling angle, and the thickness ratio of the particle.

1.3 Ice shed computation methods

Many scientific papers study the ice-particles trajectories after detachment from the wing. The 3DPM can calculate the flow field around the solid body necessary for trajectories computations (Chandrasekharan & Hinson, 2003). The other method for trajectories computation uses CFD flow field solutions using two different types of meshes: dynamic mesh like Baruzzi, Lagacé, Aubé, et Habashi (2007) and static mesh like Ignatowicz, Morency, et Lopez (2019). This section illustrates the various flow field solution methods developed for ice shedding.

Chandrasekharan and Hinson (2003) studied the ice trajectories around the Learjet 40 and Learjet 45 Bombardier aircrafts for certification. The study was carried out numerically using the 3DPM implemented in the VSAERO code to provide a necessary flow field around the solid object. Moreover, they modified the ICE program which simulated water droplet to be able to simulate solid ice particles. The location of the ice shed was specified to be the nose of the two aircrafts since the fuselages are different in length. The ice fragment wasn't chosen to shed from the wing since both aircraft has similar relative distance between the wing leading edge and the engine inlet section. For this test, the parameters to be varied are the aircraft speed, the angle of attack and the ice particle size. Relying on experimental tests, those variables were selected to study their effects on the ice trajectories. The study deduced that the ice trajectories are not affected by the fuselage length difference. The experimental test agreed with the numerical test which help decrease the simulations cost. The experimental test done on the aircraft wasn't mentioned on Chandrasekharan and Hinson paper.

Baruzzi et al. (2007) developed a new method for ice shed trajectories simulation in a uniform flow field using CFD. The study was based on Navier-Stokes analysis solved with an implicit linearization and a finite element discretization. The concept of the simulation is based on moving sub-mesh inside the main mesh connected by stitching. This is called a dynamic mesh. At each time step, the channel (it is a square sub-mesh grid represents the ice-particle) detach and by computing the new position of the particle, the channel is repositioned and reconnected to the whole domain with the removal of all overlapping. This numerical approach computes the forces in the same reference of the sub-mesh characterized by a channel and the momentum in the inertial frame of reference. Baruzzi et al. (2007) carried a 6-DOF (three rotational and three translational) analysis. Since there is a lack of references in the literature about this specific study, Baruzzi et al. used the exact analytical solution (linear displacement) by integrating Newton's second law of motion to validate their work. They used 100-time step to integrate Euler's equation of motion to calculate the angular velocity in a time t = 2 units. The lunched velocity is a unit non-dimensional velocity. The time step of each movement is Δt = 0.0001. This method, although the results match the exact solution, needs re-meshing at each time step, which implies a large computational time.

Ignatowicz et al. (2019) studied the ice trajectories around a blended wing body aircraft using a CFD flow field. A Lagrangian approach has been carried out to model the ice block movement for two ice shapes: the sphere and the flat plate. The trajectory calculation is based on the computation of the velocities anywhere in the flow field by interpolating the velocity components already calculated at the mesh nodes with CFD solution. A 3D trilinear dynamic moment model was developed based on a 2D dynamic moment model of Tachikawa (1983). The aerodynamic coefficients (the normal force coefficient which is the resultant force) are calculated based on correlations (angle of attack and side slip angle) from the literature. This model is verified with a test case, which uses a blended wing body (BWB) aircraft and was validated versus Richard et al. (2008) model. Although this is a good achievement, the computation time of one trajectory still needs 3 to 4 minutes on a core 2 Duo 16 GB RAM with CPU of 2.66 GHZ.

1.4 Monte-Carlo simulation on trajectories

The Monte-Carlo Method is a computational technique that permit a quantitative analysis of the risk for accountability of decision making. It is widely spread in many fields such as engineering, research development, transportation and environment. Monte-Carlo methods provide the researcher with a range of possible outcomes and probabilities of occurrence. It demonstrates the extreme possibility along with all consequences allowing for better decision making under uncertainties (Palisade, 2019).

Monte-Carlo simulation possess a drawback which is that it requires a huge number of computed trajectories and randomness of the initial conditions. Some researchers in the aircraft icing field used strategies to reduce the number of trajectories samples to fulfill Monte-Carlo method (Védie, Morency, & Kubler, 2016).

In the engineering field, the Monte-Carlo method is widely spread, especially when studying the uncertainty of the results. This uncertainty is caused by the randomness of the initial conditions. In civil engineering field, Nassar, Guizani, Nollet, et Tahan (2019) proposed a probability-based reliability assessment method that uses a Monte-Carlo Method to simulate the event of the simultaneous conditions of extreme events on a bridge. The methodology relies on the generation of a large number of possible realizations of the random variables of the problem, with respect to their probability distribution functions, using Monte-Carlo method. The random variables affecting the performance of the bridge are identified and assigned to distribution functions, according to the available data. The approach of Nassar et al. (2019) is very similar to the approach studied in this research.

The research on ice trajectories shed from any part of the aircraft lays down on foretelling the most probable regions where the ice particle may hit the aircraft. The probability of a trajectory crossing a plane, perpendicular to the fuselage, are drawn as iso-contours and are called footprint map. As ice particles randomly vary in size and initial velocity, a statistical study must be done to predict a probability footprint representative of the possible reality. Hence, because the probability distribution function is unknown a priori on the plane, a Monte-Carlo study is conducted to obtain the probability footprint. Then, the footprint at a specific plane downstream of the wing is used to estimate the probability distribution function in specific areas.

Suares (2005) has performed Monte-Carlo simulations on ice pieces trajectories. 60,000 trajectories were simulated to build the probability footprint. Simulations with 3 DOF (particle move along two mutual perpendicular axis and rotate along third perpendicular axis), 4 DOF (particle move along three mutual perpendicular axis and rotate around the y-axis), and 6 DOF (particle has three translational motion and three rotational motion around three perpendicular axis) model for ice particle trajectories were done. The forces and moments on the particles were computed using correlations for the aerodynamic coefficients. The shapes for the ice particles were selected to be square, rectangular and semi-circular shell. The rotational damping value was 0.0166 lb.ft.sec about the axis of rotation. A comparison was done between the trajectories in a uniform and non-uniform flow field. For the square plate, the parameters to be randomly varied are the initial lift and drag coefficient, the length, the thickness and the orientation of the particle. The results compare PDF of the trajectories footprints along z-axis, with and without damping moment coefficient applied to the ice particle. Moreover, the model was tested for iced and clean airfoil for AOA = 0 degree and AOA = 4 degrees. The input random parameters at the start of the trajectory calculation have uniform distributions. The PDF of the footprint trajectories at a plane located at the engine inlet section was shown. The 6-DOF ice-piece simulation was done for one trajectory only because of the large time needed for simulation. The results showed that the trajectory of ice-particle depend mainly on the damping coefficient, the initial orientation and the shed location.

Papadakis, Yeong, et Suares (2007) used a Monte-Carlo simulation approach for 6-DOF ice piece trajectory calculation around a business aircraft. They study footprint in a cross-section plan downstream of the wing. The plan contains the engine inlet. The study was mainly done to predict the uncertainty of the trajectory's footprint locations at the engine inlet plan. The initial parameters set up to be the shed location (side fuselage, wing), initial pitch angle and initial yaw angle of the aircraft. To obtain a PDF independent of the number of trajectories, results were compared for 10,000, 20,000, and 30,000 trajectories. The results show that for 10,000 trajectories, the footprint map in the studied plane starts to converge toward the 30,000 trajectories result, but not all the simulated trajectories will cross the plan. This happens because of the important number of trajectories which strike the aircraft parts before crossing the studied plane. Going up to 20,000 and 30,000 trajectories, the footprint map starts to give more similar results. The results also show the importance of the ice piece initial angle of attack for footprint map.

Shimoi (2010) conducted a Monte-Carlo study of the ice-piece trajectories. He compared the numerical and experimental approach to check the fidelity of the numerical technique. The experimental study uses the square, rectangular, and ice fragment shapes. The method is based on the one used by Papadakis et al. (2007) and the shed location is varied. The shed locations were chosen to be at the nose of the 3D aircraft. The shed locations also were predetermined to be as on the upper, lower and side part of the nose. The results show the effect of the shed locations on the engine inlet plan section. In this work, the number of trajectories simulated for the Monte-Carlo approach is 30,000. The ice piece shape shed from the nose was a disk with a specified thickness. The resultant aerodynamic force and momentum were calculated using the normal aerodynamic coefficients, which in turn are obtained from correlations function of angle of attack and sideslip angle.

Védie et al. (2016) performed a sensitivity analysis of the ice trajectories in 2D. Their numerical method lies on using Newton's second law of motion in a Lagrangian frame by an adaptive Runge-Kutta method. Correlations were used from Holmes et al. (2006) to calculate lift, drag, moment and magnus effect. Their results were validated against the literature. Moreover, many random trajectories were simulated based on the randomness of the initial parameters: initial velocity, angular velocity and initial rotation angle. The convergence of the Monte-Carlo method for a uniform norm error was achieved at 800 000 trajectories. Furthermore, they predicted a way to reduce the Monte-Carlo method iterations by setting a convergence criteria for the mean trajectory. The convergence is attained by obtaining a mean error of 0.001 and a variance error of 0.1 for the mean trajectory. This stopping criteria was proficient to decrease the number of simulated trajectories from 800 000 to 6130 trajectories at its maximum case.

The review of literature illustrates the effect of icing and de-icing on the aircraft and its consequences. The state of the art shown above pointed out the main methods for trajectory computations, the models for trajectory's simulations and the Monte-Carlo simulations procedure to obtain a footprint map. There are two different methods to compute flow field solutions for trajectory's computation: The Panel Method by programs provided by NASA and other researchers or CFD solution using static or dynamic mesh.

Most trajectory calculation methods rely on Newton second law and aerodynamic coefficients. Also, the number of trajectory needed for good footprint map is not clear, ranging from a few hundred to more than 30000. The previous studies in icing did mention a method to reduce the number of trajectories simulated to fulfill Monte-Carlo simulation in 2D but not in 3D.

CHAPTER 2

MATHEMATICAL MODELING AND NUMERICAL METHOD

This chapter treats the methodology used for the ice particle computations. There are three sub-sections in this chapter. Firstly, the model for the flow field calculations using 3DPM is explained. Secondly, the methodology to calculate the trajectories in the corresponding flow field is illustrated as well as the implementation of these equations in MATLAB. Finally, a Monte-Carlo method to obtain the footprint map data is explained.

2.1 3D panel method

2.1.1 3D potential flow over a wing

The panel method used in the current research follows the one used by Katz et Plotkin (2001). This method considers a non-uniform flow field, having a wake. The flow is considered incompressible, inviscid and irrotational. The potential flow around the solid body is defined by the summation of the perturbation potential velocity and the uniform velocity calculated in the equation (2.1) (Katz & Plotkin, 2001).

$$\Phi = \phi + \Phi_\infty \tag{2.1}$$

where Φ_∞ is the fluid potential calculated using the equation (2.2).

$$\begin{gathered} \Phi_\infty = U_\infty x + V_\infty \mathrm{y} + W_\infty z \\ U = U_\infty . \cos(a) \\ W = W_\infty . \sin(a) \end{gathered} \tag{2.2}$$

With a is the angle of attack. V_∞ doesn't exist in the equation since the side slip angle with respect to the flow is considered as zero. The velocity of the flow field derives from a potential which fulfill the Laplace equation stated as follows, equation (2.3) (Ashby et al., 1991).

$$\nabla^2\Phi = 0 \tag{2.3}$$

Equation (2.3) is solved assuming three boundary conditions (Tarafder, Saha, & Mehedi, 2010):

- Firstly, the velocity vector component which is normal to the solid boundaries of the airfoil must be zero:

$$\nabla\Phi.\mathbf{n} = 0 \tag{2.4}$$

- Secondly, the disturbance induced will decay away from the solid body as (Q_∞ is the freestream velocity):

$$\lim_{r\to\infty} \nabla\Phi = \boldsymbol{Q}_\infty \tag{2.5}$$

- Thirdly, the solution should satisfy the Kutta-condition at the trailing edge of the lifting body such that the potential jump across the wake surface S_w is the same as the circulation Γ.

$$[\Delta\Phi]_{on\, S_w} = \Gamma = constant = \Delta\Phi_{T.E.} \tag{2.6}$$

2.1.2 Solution by Green's identity

A three-dimensional flow is considered around the wing. The Laplace equation (2.3) can be solved in a three-dimensional domain Ω. A boundary S is considered and divided into three sub-domains: S_B, S_w, S_∞. S_B refers to the solid body, S_w refers to the wake which is considered constant for the rest of the calculations and always parallel to the chord even when changing the angle of attack, and S_∞ refers to the farfield. The vector normal **n** is always pointing outside the region of interest. A random point P is taken with coordinates $P\ (x, y, z)$ away from a point $q\ (\xi, \eta, \zeta)$ with a distance r between P and q. This domain is shown in the figure (2.1).

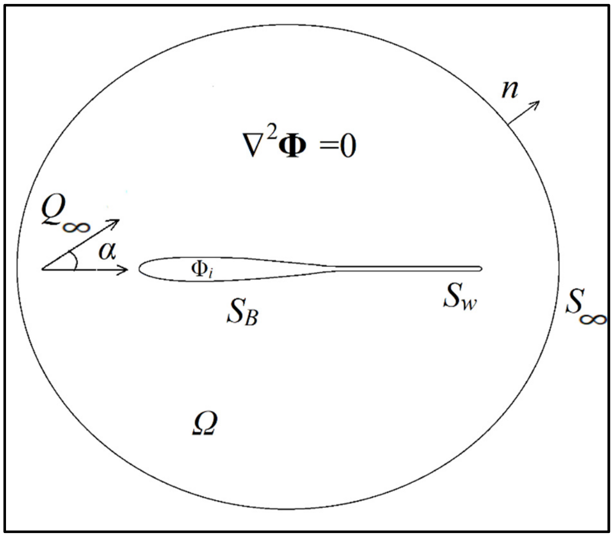

Figure 2.1 Potential flow around a solid body
inspired by Katz et Plotkin (2001)

Thus, the equation (2.3) will turn into equation (2.7) to find the potential velocity at the point *P,* (Katz & Plotkin, 2001).

$$\Phi(\mathrm{P}) = \frac{1}{4\pi}\int_{S_B} \left[\frac{1}{\mathrm{r}}\nabla(\Phi - \Phi_\mathrm{i}) - (\Phi - \Phi_\mathrm{i})\nabla\frac{1}{\mathrm{r}}\right].\mathbf{n}\,\mathrm{dS} - \frac{1}{4\pi}\int_{S_w} \Phi\mathbf{n}.\nabla\frac{1}{\mathrm{r}}\,\mathrm{dS} + \Phi_\infty(\mathrm{P}) \tag{2.7}$$

with Φ_i the inner surface potential. The difference between the inner and external potentials and the difference between their derivatives with respect to the normal vector are respectively shown in equations (2.8) and (2.9) (Katz & Plotkin, 2001).

$$-\mu = \Phi - \Phi_\mathrm{i} \tag{2.8}$$

$$-\sigma = \frac{\partial\Phi}{\partial n} - \frac{\partial\Phi_\mathrm{i}}{\partial n} \tag{2.9}$$

with μ and σ are the doublet and source respectively. The minus sign is a result of the normal vector *n* pointing into S_B. In this case, equation (2.7) can be re-written in equation (2.10) (Katz & Plotkin, 2001).

$$\Phi(\mathrm{P}) = -\frac{1}{4\pi}\int_{S_B}^{\cdot}\left[\sigma\frac{1}{\mathrm{r}} - \mu\frac{\partial}{\partial \mathrm{n}}\frac{1}{\mathrm{r}}\right] dS + \frac{1}{4\pi}\int_{S_w}^{\cdot}\left[\mu\frac{\partial}{\partial \mathrm{n}}\frac{1}{\mathrm{r}}\right] dS + \Phi_\infty(\mathrm{P}) \qquad (2.10)$$

2.1.3 Dirichlet boundary conditions

To solve the system of equations, the Dirichlet boundary conditions are imposed. The Dirichlet boundary conditions stated that the perturbation potential at S_B should be specified and the zero-flow normal to the surface is to be specified in terms of velocity potential as in equation (2.11) (Katz & Plotkin, 2001).

$$\Phi_i = (\phi + \Phi_\infty)_i = const \qquad (2.11)$$

The inner potential Φ_i with respect to the point *P (x, y, z)* inside the surface S_B is calculated in equation (2.12)(Katz & Plotkin, 2001).

$$\Phi_i(\mathrm{P}) = \frac{1}{4\pi}\int_{S_B+S_W}^{\cdot}\left[\mu\frac{\partial}{\partial \mathrm{n}}\frac{1}{\mathrm{r}}\right] dS - \frac{1}{4\pi}\int_{S_B}^{\cdot}\left[\sigma\frac{1}{\mathrm{r}}\right] dS + \Phi_\infty \qquad (2.12)$$

Pointing out that when $r \to 0$, both integrals will tend to singularity, and near this value, the integrals must be evaluated. The boundary condition inside the surface at any point becomes as shown in equation (2.13) (Katz & Plotkin, 2001).

$$\frac{1}{4\pi}\int_{S_B+S_W}^{\cdot}\left[\mu\frac{\partial}{\partial \mathrm{n}}\frac{1}{\mathrm{r}}\right] dS - \frac{1}{4\pi}\int_{S_B}^{\cdot}\left[\sigma\frac{1}{\mathrm{r}}\right] dS + \Phi_\infty = const \qquad (2.13)$$

The equation (2.13) is very important because now the surface of the solid body can be discretized into *N* panels and the integration for each panel is done by equation (2.14) (Katz & Plotkin, 2001).

$$\frac{1}{4\pi}\sum_{j=1}^{N}\int\left[\mu\frac{\partial}{\partial \mathrm{n}}\frac{1}{\mathrm{r}}\right]dS-\frac{1}{4\pi}\sum_{j=1}^{N}\int\left[\sigma\frac{1}{\mathrm{r}}\right]dS+\Phi_{\infty}=const \tag{2.14}$$

The integration now is limited to each individual panel element. But it's necessary to mention the influence of panel *j* at a random point *P* which is computed in function of doublet and source respectively as shown in equation (2.15) (Katz & Plotkin, 2001).

$$\begin{gathered}\frac{1}{4\pi}\int\left[\frac{\partial}{\partial \mathrm{n}}\frac{1}{\mathrm{r}}dS\right]_j\equiv C_j\\ -\frac{1}{4\pi}\int\left[\frac{1}{\mathrm{r}}dS\right]_j\equiv B_j\end{gathered} \tag{2.15}$$

Finally, the boundary condition in equation (2.13) allows the creation of *N* linear equations based on *N* collocation points. This boundary condition is represented in the equation (2.16) (Katz & Plotkin, 2001).

$$\sum_{j=1}^{N}B_j\sigma_j+\sum_{j=1}^{N}C_j\mu_j+\Phi_{\infty}=const \tag{2.16}$$

2.1.4 Influence coefficient calculation

The 3D panel method used combines the source and doublet. That means, every panel has a local constant source and doublet strength. Since the Dirichlet boundary conditions are used and the equation (2.16) is not unique, the strength source is fixed to get a set of equations with the unknown doublet strengths. Thus, the equation (2.17) calculates the source strength after Katz & Plotkin (2001).

$$\sigma_j=n\,.\;Q_{\infty} \tag{2.17}$$

The boundary condition will reduce after setting the inner perturbation velocity equal to Φ_{∞} and will become, as shown in equation (2.18) (Tarafder et al., 2010).

$$\sum_{j=1}^{N} B_j\sigma_j + \sum_{j=1}^{N} C_j\mu_j = 0 \tag{2.18}$$

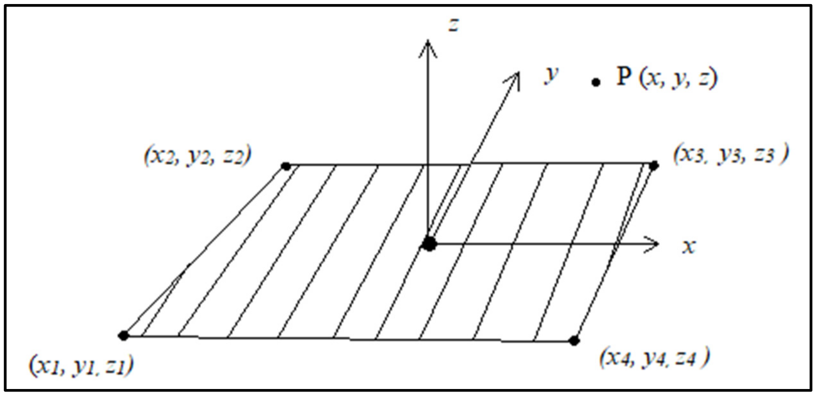

Figure 2.2 Quadrilateral panel (Katz & Plotkin, 2001).

Figure 2.2 shows the panel vertex coordinates ($x_1, x_2, x_3, x_4, y_1, y_2, y_3, y_4, z_1, z_2, z_3, z_4$), the x, y, z are the coordinates of influenced arbitrary field point *P* in space. The local frame of reference of the panel is shown.

Consider a wake panel that is shed by an upper panel and a lower panel as shown in the figure (2.3). The equation of the first collocation point where it includes the influence coefficients, source and doublet parameter of each panel can be derived as shown in equation (2.19) (Katz et Plotkin, 2001).

$$C_{11}\mu_N + \cdots + C_{1N}\mu_N + \cdots + C_{1l}\mu_l + \cdots + C_{1l}\mu_l + \sum_{p=1}^{N_w} C_{1P}\mu_P + \sum_{k=1}^{N} B_{1j}\sigma_j = 0 \tag{2.19}$$

Figure 2.3 demonstrates the Kutta-condition on trailing edge. This will add another equation to the panel’s matrix. The Kutta-condition is used to calculate the doublet at the wake panel which will remain constant for the rest of the wake panels decaying away from the trailing edge of the wing. The doublet of the wake panel is the difference between the upper and lower doublet, as shown in equation (2.20).

$$\mu_w = \mu_N - \mu_l \tag{2.20}$$

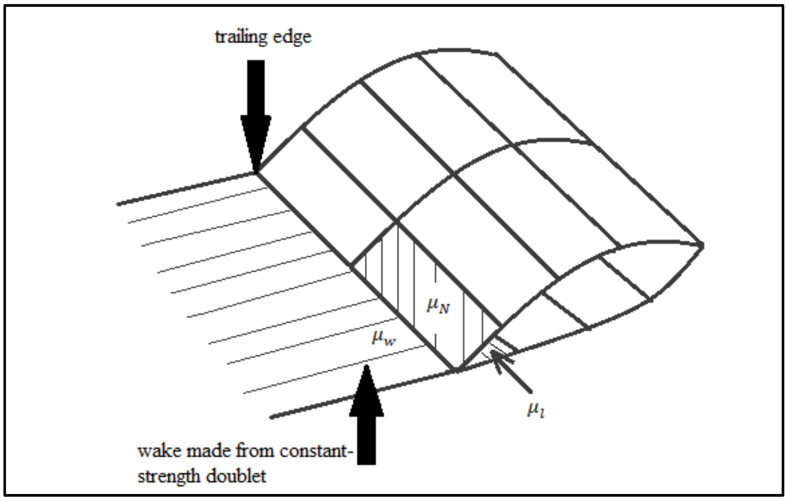

Figure 2.3 Kutta condition at the trailing edge (Katz & Plotkin, 2001)

The previous equation (2.19) consists of N equations with N+1 unknown, where N is the number of panels. The Kutta-condition is used to add the N+1 equation to the matrix of N equations with N+1 unknowns. Equation (2.19) will transform into equation (2.21).

$$C_{11}\mu_N + \cdots + (C_{1N} + C_{1p})\mu_N + \cdots + (C_{1l} - C_{1p})\mu_l + \cdots + C_N\mu_N + \sum_{k=1}^{N} B_{1j}\sigma_j = 0 \tag{2.21}$$

The equation (2.21) can be simplified into equation (2.22).

$$\sum_{k=1}^{N} A_{1j}\mu_j = -\sum_{k=1}^{N} B_{1j}\sigma_j \tag{2.22}$$

Since the wake shedding is not taken into account, then $A_{1j}= C_{1j}$. In matrix form, equation (2.22) will transform into equation (2.23).

$$\begin{pmatrix} a_{11} & a_{12} & \cdots & a_{1N} \\ a_{12} & a_{22} & \dots & a_{2N} \\ a_{13} & a_{32} & \dots & a_{3N} \\ \vdots & & \ddots & \vdots \\ a_{N2} & a_{N2} & \cdots & a_{NN} \end{pmatrix} \begin{pmatrix} \mu_1 \\ \mu_2 \\ \mu_3 \\ \vdots \\ \mu_N \end{pmatrix} = - \begin{pmatrix} b_{11} & b_{12} & \cdots & b_{1N} \\ b_{12} & b_{22} & \dots & b_{2N} \\ b_{13} & b_{32} & \dots & b_{3N} \\ \vdots & & \ddots & \vdots \\ b_{N2} & b_{N2} & \cdots & b_{NN} \end{pmatrix} \begin{pmatrix} \sigma_1 \\ \sigma_2 \\ \sigma_3 \\ \vdots \\ \sigma_N \end{pmatrix} \tag{2.23}$$

This matrix represents a set of N linear equations with N unknown. Note that A_{jj}=0.5 on the diagonal of the panel except when the panel is at the edge of the trailing edge (Katz & Plotkin,2001). Since the source strength is known (equation 2.17) then we can establish a right-hand side matrix, and this will be shown in the equation (2.24).

$$\begin{pmatrix} a_{11} & a_{12} & \cdots & a_{1N} \\ a_{12} & a_{22} & \dots & a_{2N} \\ a_{13} & a_{32} & \dots & a_{3N} \\ \vdots & & \ddots & \vdots \\ a_{N2} & a_{N2} & \cdots & a_{NN} \end{pmatrix} \begin{pmatrix} \mu_1 \\ \mu_2 \\ \mu_3 \\ \vdots \\ \mu_N \end{pmatrix} = \begin{pmatrix} RHS_1 \\ RHS_2 \\ RHS_3 \\ \vdots \\ RHS_N \end{pmatrix} \tag{2.24}$$

2.1.5 Computations of surface velocities and pressure

The interest of this method for this study is its ability to compute surface velocities and the velocities everywhere in the flow field, and the parametric aerodynamic coefficients on the solid body. After calculating the strength of the doublet, the potential velocity outside the surface is calculated. There are two perturbation velocity directions: the normal q_n and the tangential q_l , q_m components. These components are shown in the equations (2.25) respectively (Katz & Plotkin, 2001).

$$\begin{aligned} q_n &= \sigma \\ q_l &= -\frac{\partial \mu}{\partial l} \\ q_m &= -\frac{\partial \mu}{\partial m} \end{aligned} \tag{2.25}$$

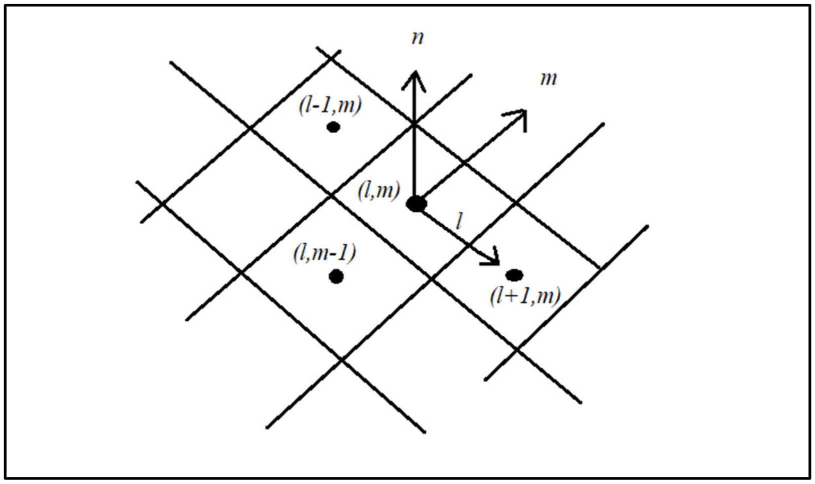

Figure 2.4 Panel local coordinate system to evaluate the tangential velocity components

The velocity component in *l* direction, equation (2.26).

$$q_l = \frac{1}{2\Delta l}(\mu_{l-1} - \mu_{l+1}) \tag{2.26}$$

where Δl, is the panel length in the *l* direction. The total velocity at a collocation point *N* is the summation of the free stream velocity and the perturbation velocity, equation (2.27).

$$Q_i = (Q_{\infty l}, Q_{\infty m} Q_{\infty n})_i + (q_l, q_m, q_n)_i \tag{2.27}$$

The pressure coefficient for each panel is calculated by equation (2.28).

$$C_{PN} = 1 - \frac{Q_i^2}{Q_\infty} \tag{2.28}$$

Equation (2.28) calculates the aerodynamic pressure coefficient on one panel. The total aerodynamic load is calculated by adding all aerodynamic loads for each panel together.

2.1.6 Velocity calculations in the farfield

With the known source and doublet element at each panel from the previous calculations, Katz et Plotkin (2001) identified a way to calculate the velocity at an arbitrary point in the farfield.. The source and doublet at each panel influence the velocity in the near field. Thus, the velocity of the arbitrary point *P (x, y, z)* could be calculated from the velocity potential, when the distance is about 3-5 times larger than the panel size, as follow (Katz & Plotkin, 2001).

$$\Phi s_{(x,y,z)} = \frac{-\sigma A}{4\pi\sqrt{(x-x_0)^2+(y-y_0)^2+(z-z_0)^2}}$$

$$\Phi d_{(x,y,z)} = \frac{-\mu A z}{4\pi . \sqrt[3]{(x-x_0)^2+(y-y_0)^2+(z-z_0)^2}} \tag{2.29}$$

With Φs and Φd are the potential flow due to source and doublet respectively, σ is the source element, μ is the doublet element, *A* is the panel area, *(x, y, z)* are the coordinate of the point of interest *P* in the farfield, (x_0, y_0, z_0) are the collocation point coordinate of the panel ($z_0 = 0$). Equation (2.29) applies when the distance is 3-5 times bigger than the panel diameter. Bear in mind that this equation is set up for one panel. Since the wing possesses more than one panel then the summation of those influenced velocities at the point *P* will be considered. On the wing surface, the velocities are known but in the farfield, the velocity components based on the source element are calculated with equation (2.30) (Katz & Plotkin, 2001).

$$u_s(x,y,z) = \frac{\sigma A(x-x_0)}{4\pi[(x-x_0)^2+(y-y_0)^2+z^2]^{3/2}}$$

$$v_s(x,y,z) = \frac{\sigma A(y-y_0)}{4\pi[(x-x_0)^2+(y-y_0)^2+z^2]^{3/2}} \tag{2.30}$$

$$w_s(x,y,z) = \frac{\sigma A(z-z_0)}{4\pi[(x-x_0)^2+(y-y_0)^2+z^2]^{3/2}}$$

(u_s, v_s, w_s) are the coordinates of the velocity potential due to source, (x_0, y_0, z_0) are the collocation point coordinates for each panel and A is the panel area. In the farfield, the velocity components based on the doublet element are, (Katz & Plotkin, 2001) equation (2.31).

$$u_d(x,y,z) = \frac{3\mu A(x-x_0)z}{4\pi[(x-x_0)^2+(y-y_0)^2+z^2]^{5/2}}$$
$$v_d(x,y,z) = \frac{3\mu A(y-y_0)z}{4\pi[(x-x_0)^2+(y-y_0)^2+z^2]^{5/2}} \tag{2.31}$$
$$w_d(x,y,z) = -\frac{\mu A[(x-x_0)^2+(y-y_0)^2-2z^2]}{4\pi[(x-x_0)^2+(y-y_0)^2+z^2]^{5/2}}$$

The velocity components due to the doublet element (u_d, v_d, w_d) are obtained by differentiating the equation (2.29) with respect to (*x, y, z*) respectively. Then, those three velocity components (due to source and doublet) will be subtracted from the flow velocity components to form the fluid velocity (Ashby et al., 1991), equation (2.32).

$$U_{total}(x,y,z) = Ut - u_s(x,y,z) - u_d(x,y,z)$$
$$V_{total}(x,y,z) = Vt - v_s(x,y,z) - v_d(x,y,z) \tag{2.32}$$
$$W_{total}(x,y,z) = Wt - w_s(x,y,z) - w_d(x,y,z)$$

Ut, *Vt* and *Wt* are the free stream velocity components in (*x, y, z*) direction respectively which are respectively equal to Q_∞ components with respect to the global frame of reference.

2.1.7 Closing the wing tip

The mesh generated by the 3DPM program available in the annexes of the book by Katz et Plotkin (2001) has an open wing tip. A wing with an open wing tip generates a lift force coefficient that is not linear with respect to the angle of attack. To solve this problem a correction is made to the book program such as to close the wing tip. The aim is to correct the flow around the wing tip. Since the flow solution depends on the calculations of the parameters at each panel, then a correction of the flow at the tip will affect the whole solution. Next figures 2.5 and 2.7 shows the geometry generated by the 3DPM code before and after closing the wing tip.

Figure 2.5 shows how the program creates a wing from IB+1 airfoil coordinates, which is read from a file. Note that IB+1 is the number of the coordinates of the airfoil. The x and z coordinates are given in anticlockwise order around the airfoil, with a duplicated node at wing tip. Thus, the coordinates of node 1 should be the same as coordinates of node IB+1.

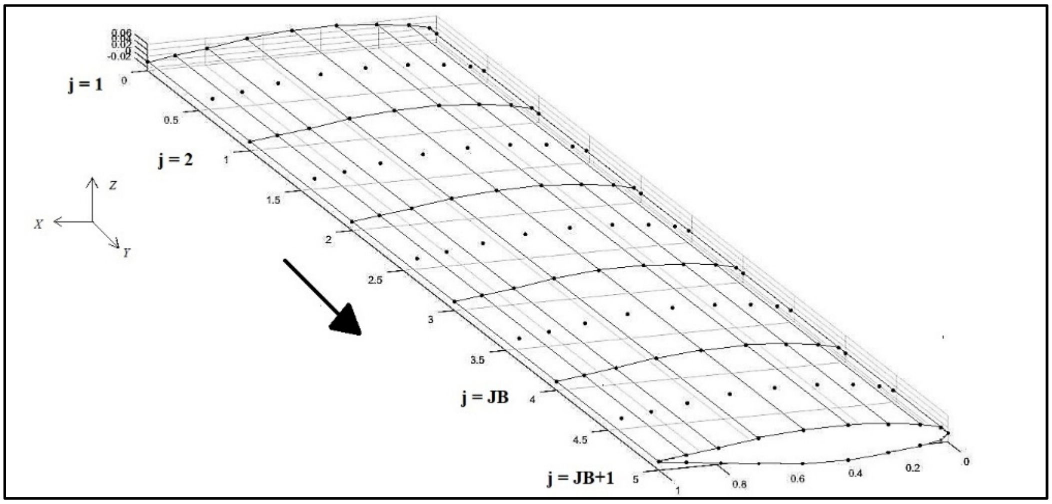

Figure 2.5 Wing before closing the wing tip

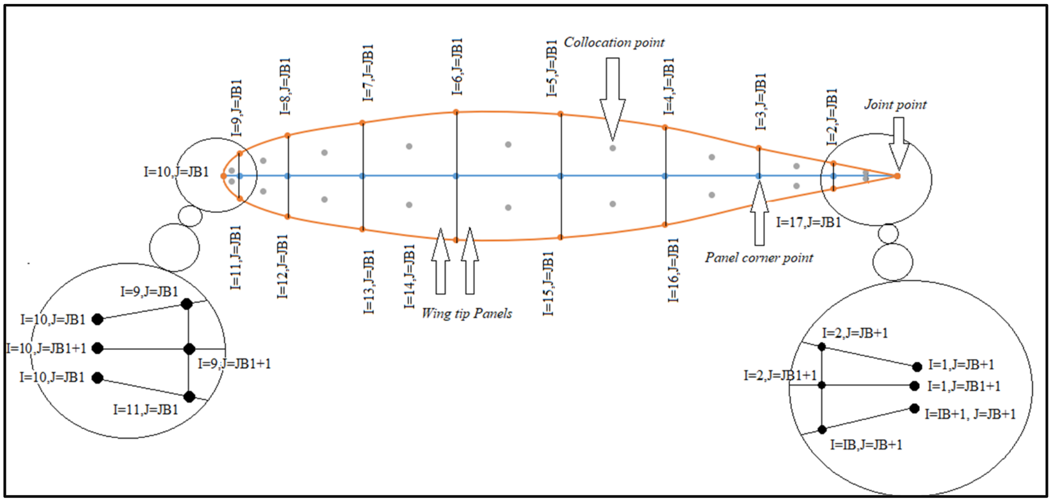

Figure 2.6 Strategy for closing the wing tip by adding some panels.

Figure 2.6 presents the airfoil at the tip section. The panels are quadrilateral. The counter I stands for the X direction while J is for Y direction. The coordinates of the wing are represented as from 1 to IB+1. The wing spanwise sections are represented from 1 to JB+1 starting from the root section along the tip. This step enables to create corner points on the airfoil creating the corner stones of the panels. In addition, based on the corner point calculation, the collocation points, which are located in the center of each panel are created. Two specific points should be mentioned: at the trailing edge and at the leading edge. At the trailing edge and leading edge, the panel points are superposed. The first and last point of the counter are also separated. In this case, the program will treat the panel as quadrilateral with a size of length 0, and not triangular. It is necessary to mention that the strength and doublet formulation allow a length of 0. The wing tip closure will correct slightly the flow and affect the pressure and lift coefficients.

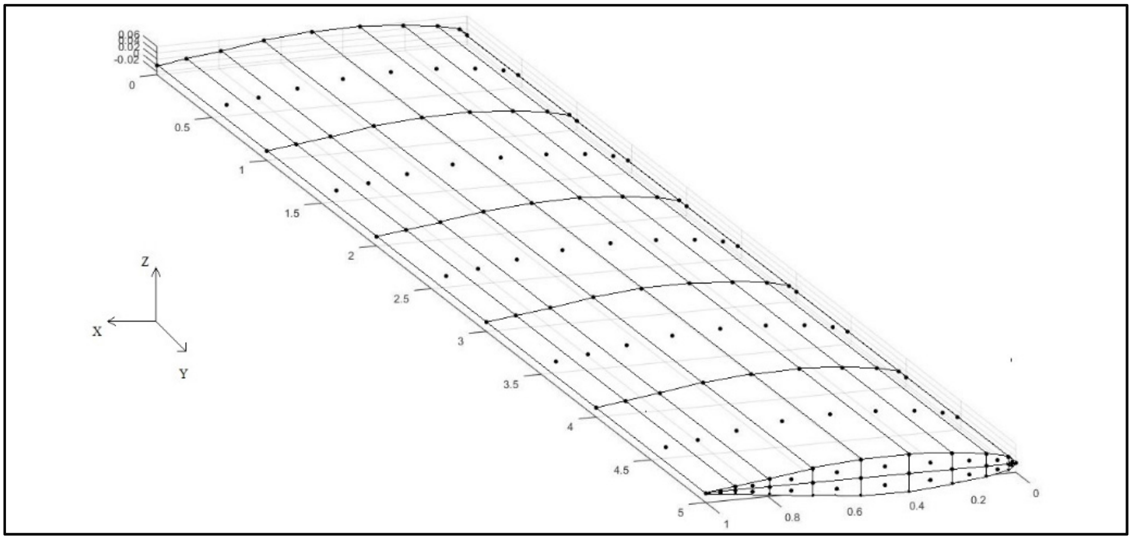

Figure 2.7 Wing after closing the wingtip.

The figure 2.7 shows the wing with closed wingtip, with the QF node coordinate at span position J=JB+1=JB1. The corner points coordinates are stored in QF (I, J, 1-3) from I=1 to I=IB+1=IB1. To close the tip, nodes should be added along the camber line such that the wing tip panels can be created. These node coordinates will be stored in QF at J=JB+2=JB2. The new coordinates are obtained by taking the middle position between upper nodes and lower nodes. It is thus necessary to have the same number of nodes on the upper side and the lower side of the airfoil. As mentioned, the panels consist of corner points and collocation points. Let's consider that the coordinates of the airfoil at the wing tip are called as (X_t, Y_t, Z_t), where *t* tends to tip section and *n* tends to the number of airfoil coordinates. So, the additional corner points could be found by the summation of the top point of the airfoil coordinate plus the lower point divided by two. Thus, at the tip, the corner points are calculated as follows, equation (2.33).

$$\begin{aligned}
X_{tip(1,2,\ldots n)} &= \frac{X_{t(1,2,3\ \ldots\ \frac{n}{2})} + X_{t(n,(n-1),(n-2)\ \ldots\ \frac{n}{2})}}{2} \\
Y_{tip(1,2,\ldots n)} &= \frac{Y_{t(1,2,3\ \ldots\ \frac{n}{2})} + Y_{t(n,(n-1),(n-2)\ \ldots\ \frac{n}{2})}}{2} \qquad (2.33) \\
Z_{tip(1,2,\ldots n)} &= \frac{Z_{t(1,2,3,\ \ldots\ \frac{n}{2})} + Z_{t(n,(n-1),(n-2)\ \ldots\ \frac{n}{2})}}{2}
\end{aligned}$$

where $(X_{tip}, Y_{tip}, Z_{tip})$ is the new coordinates of the tip panel corner points, and (X_t, Y_t, Z_t) are the corner points coordinates at the wing tip section. The collocation point is at the center of the panel, calculated by the equation (2.34).

$$\begin{aligned} X_{ctip\,(1,2,3,\ldots,n)} &= \frac{X_{tip(1,2,3,\ldots,n)} + X_{tip(2,3,4\ldots n+1)} + X_{t(1,2,3,\ldots,n)} + X_{t(2,3,4,\ldots n+1)}}{4} \\ Y_{ctip\,(1,2,3,\ldots,n)} &= \frac{Y_{tip(1,2,3,\ldots,n)} + Y_{tip(2,3,4\ldots n+1)} + Y_{t(1,2,3,\ldots,n)} + Y_{t(2,3,4,\ldots n+1)}}{4} \\ Z_{ctip\,(1,2,3,\ldots,n)} &= \frac{Z_{tip(1,2,3,\ldots,n)} + Z_{tip(2,3,4\ldots n+1)} + Z_{t(1,2,3,\ldots,n)} + Z_{t(2,3,4,\ldots n+1)}}{4} \end{aligned} \tag{2.34}$$

where, $(X_{ctip}, Y_{ctip}, Z_{ctip})$ are the new collocation points coordinates of the tip panels. Note that after adding the tip panels, the parameters like doublet and source are also calculated and added to the wing surface panels using the equation (2.24) mentioned before in section 2.1.

2.2 Trajectories simulations

In the previous section (2.1), the 3DPM provided all the necessary parameters and flow field information for the problem. Now in this section, a trajectory computation strategy will be held. Before presenting the trajectory calculation model, the definitions for the frame of references are required. A fixed or global frame of reference and local frame of reference for the particle are represented respectively as (X, Y, Z) and (Xp, Yp, Zp). The velocities are divided into two: the velocity of the particle in the global frame of reference noted as (Up, Vp, Wp), and the velocity of the fluid (air) in the global frame of reference noted as $(U_{total}, V_{total}, W_{total})$ calculated in section 2.1 equation (2.32). The relative velocity $\boldsymbol{V_{re}} = [Ur; Vr; Wr]$ of the particle in the global frame of reference is calculated as following, equation (2.35).

$$\begin{aligned} U_r &= U_{total} - Up \\ V_r &= V_{total} - Vp \\ W_r &= W_{total} - Wp \end{aligned} \tag{2.35}$$

To calculate the trajectory of the particle in space, the Newton's second law of motion is applied to the particle, equation (2.36). An illustration of the forces applied to the particle is shown in figure 2.8.

$$\sum \vec{F} = m\vec{a} \tag{2.36}$$

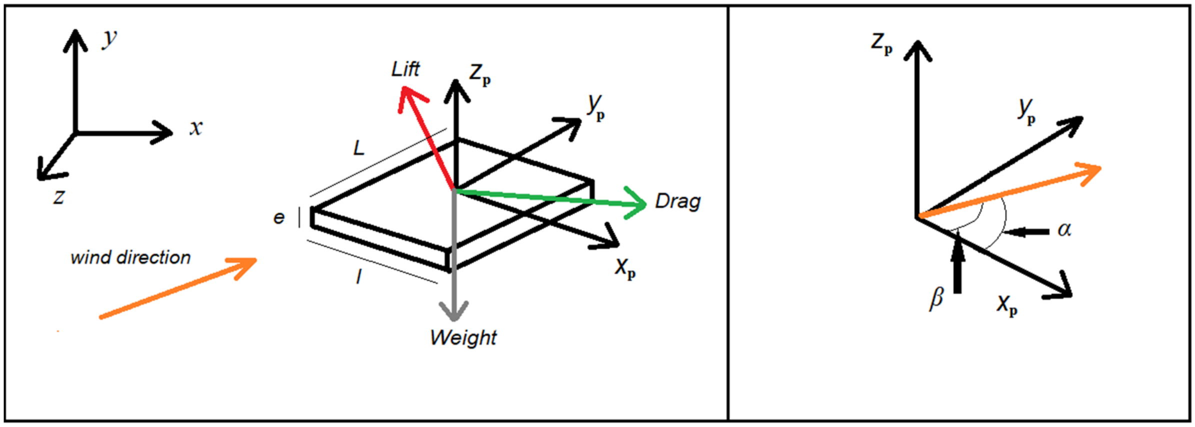

Figure 2.8 Forces applied to the particle with respect to the relative wind velocity

The figure 2.8 represents the ice particle characteristics. *L* is the length, *l* is the width and *e* is the thickness of the particle. The local and the global frame of reference are also shown. The aerodynamic forces as well as the wind direction are illustrated. To integrate the equation of motion with respect to the global frame of reference axis, the equation (2.36) will transform into equation (2.37).

$$\begin{gathered} Fx = m\frac{dU_p}{dt} \\ Fy = m\frac{dV_p}{dt} \\ Fz = m\frac{dW_p}{dt} - mg \end{gathered} \tag{2.37}$$

This expression involves the following terms:

- Fx, Fy, Fz are the projections of the forces in the x, y, and z axis (N).
- m is the mass of the particle (kg).
- g is the gravitational force which is 9.81 (m/s^2).

The position of the particle is determined by integrating two times the acceleration of the particle with respect to time. The positions of the particle at each time step construct the particle path. While moving, the particle rotates in different directions with respect to the three local main axis. The orientation of the particle is defined by three angles called Euler's angles: rolling, pitching and yawing moment are associated to Φ, θ and Ψ which are the angles of rotation around X_p, Y_p and Z_p respectively. The moments applied to the particle are the pitching, yawing, and rolling moment. The equation of moment is represented by the following, equation (2.38) (Ignatowicz et al., 2019).

$$I\begin{bmatrix}\dot{P}\\\dot{Q}\\\dot{R}\end{bmatrix} = \boldsymbol{M_t} - \begin{bmatrix}P\\Q\\R\end{bmatrix} \times I\begin{bmatrix}P\\Q\\R\end{bmatrix} \tag{2.38}$$

This expression involves the following terms:

- I is matrix of inertia ($kg.m^2$).
- $\boldsymbol{\Omega} = \begin{bmatrix}P\\Q\\R\end{bmatrix}$ the angular velocity of the local frame of reference (rad/s).
- $\boldsymbol{M_t}$ the total moment of the particle of the local frame of reference (N.m).
- × is the cross product operator.

To calculate the aerodynamic forces at each time step is a complex task to do. That's why a simplified solution is provided by Richards, Williams, Laing, McCarty, et Pond (2008). They claim to reduce the forces computation time and introduce a new resultant normal aerodynamic force $\mathbf{F_{np}}$ directed perpendicular to the flat plate in the positive direction of the z-axis from the center of pressure of the particle. The resultant normal force is expressed by equation (2.39).

$$F_{np} = 0.5\rho|\boldsymbol{V_{re}}|^2 L l C_N \tag{2.39}$$

The parameters of this equation are as follows:

- ρ is the density of the air (kg/m^3).

- $\boldsymbol{V_{re}}$ is the relative velocity in the local frame of reference (m/s).
- C_N is the normal resultant force coefficient.
- L and l are the length and width of the flat plate (m).

Figure 2.9 depicts the particle motion. The two frames of references are shown: the general frame of reference and the particle local frame of reference. The center of gravity lies at the same point as the geometrical center of the particle because the particle is assumed to be a rectangular homogenous flat plate. The center of pressure shown in the picture is not the real fixed point but to show that most of the time the center of gravity and the center of pressure are not at the same point.

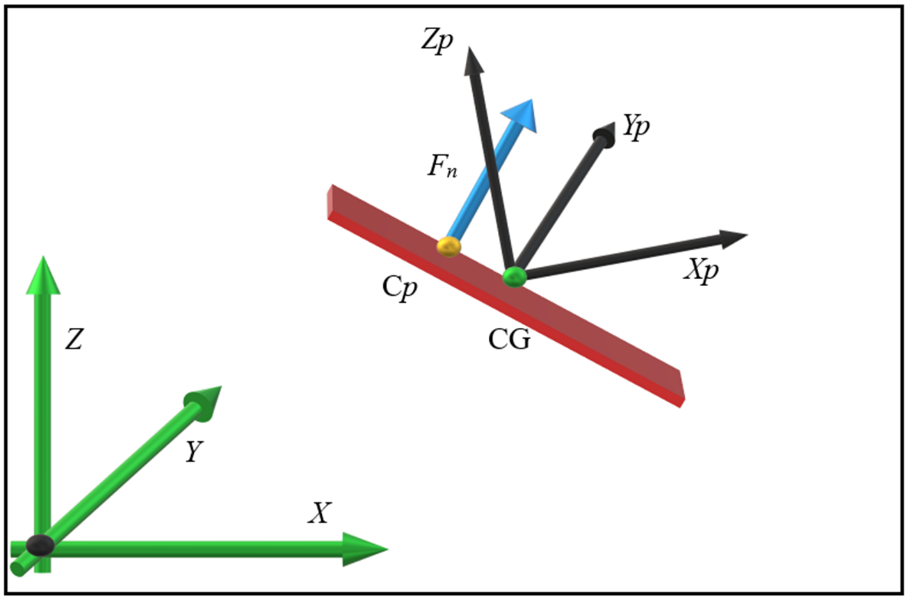

Figure 2.9 Motion of the flat plate representation

The normal force coefficient is found through experiments by Richards et al. (2008). Richards has been working to find out that the normal force coefficient depends on the side slip angle β and the angle of attack α. The angle of attack and the side slip angle is calculated as follows in equation (2.40) and presented in figure 2.8 (Richards et al., 2008).

$$\alpha = arcsin\left(\frac{W_r}{|\boldsymbol{V_{re}}|}\right)$$
$$\beta = arcsin\left(\frac{V_r}{|\boldsymbol{V_{re}}|\cos(\alpha)}\right) \tag{2.40}$$

Richards et al. (2008) founds also that the normal force coefficient also depends on the surface ratio of the flat plate. The surface ratio of the flat plate is defined to be the length over the width of the same flat plate. By adjusting the surface ratio of the flat plate and calculating the angle of attack and side slip angle, the C_N is finally found by interpolation through these correlations. Once the force is expressed in the local frame of reference of the plate, $\mathbf{F_{np}}$ is then being transformed to the general frame of reference and thus equation (2.39) is solved.

The classic transformation of the vector force from local particle frame of reference to the global frame of reference is done through Euler's transformation. This transformation is done through a transformation matrix we called it $R_q(q)$. For instance, the transformation of the velocity vector is done by the equation (2.41). This transformation is done using Euler's angles.

$$\boldsymbol{V_{re}} = R_q(q)\boldsymbol{V_g}$$
$$\boldsymbol{V_g} = R_q(q)^{-1}\boldsymbol{V_{re}} \tag{2.41}$$

$$R_q(q) = \begin{bmatrix} q_1^2 + q_2^2 - q_3^2 - q_4^2 & 2q_2q_3 + 2q_1q_4 & 2q_2q_4 - 2q_1q_3 \\ 2q_2q_3 - 2q_1q_4 & q_1^2 - q_2^2 + q_3^2 - q_4^2 & 2q_3q_4 + 2q_1q_2 \\ 2q_2q_4 + 2q_1q_3 & 2q_3q_4 - 2q_1q_2 & q_1^2 - q_2^2 - q_3^2 + q_4^2 \end{bmatrix} \tag{2.42}$$

$\boldsymbol{V_g}$ is the velocity vector in the local frame of reference of the particle. $R_q(q)$ is a matrix which depends on the quaternions calculated in equation (2.43). The quaternions will model the rotation of the particle around a single axis which is directed by a unit vector. The quaternions are four scalar expressions that depends on Euler's angles which characterize the orientation of the particle at every rotation (Fu, Huang, & Gu, 2013) (Diebel, 2006). These relations are expressed by the equation (2.43).

$$\begin{aligned} q_1 &= \cos\left(\frac{\Phi}{2}\right)\cos\left(\frac{\theta}{2}\right)\cos\left(\frac{\Psi}{2}\right)+\sin\left(\frac{\Phi}{2}\right)\sin\left(\frac{\theta}{2}\right)\sin\left(\frac{\Psi}{2}\right) \\ q_2 &= \cos\left(\frac{\Phi}{2}\right)\sin\left(\frac{\theta}{2}\right)\sin\left(\frac{\Psi}{2}\right)-\sin\left(\frac{\Phi}{2}\right)\cos\left(\frac{\theta}{2}\right)\cos\left(\frac{\Psi}{2}\right) \\ q_3 &= -\cos\left(\frac{\Phi}{2}\right)\sin\left(\frac{\theta}{2}\right)\cos\left(\frac{\Psi}{2}\right)-\sin\left(\frac{\Phi}{2}\right)\cos\left(\frac{\theta}{2}\right)\sin\left(\frac{\Psi}{2}\right) \\ q_4 &= \sin\left(\frac{\Phi}{2}\right)\sin\left(\frac{\theta}{2}\right)\cos\left(\frac{\Psi}{2}\right)-\cos\left(\frac{\Phi}{2}\right)\cos\left(\frac{\theta}{2}\right)\sin\left(\frac{\Psi}{2}\right) \end{aligned} \tag{2.43}$$

The aerodynamic forces pass through the center of pressure. To solve the moment equation (2.38) the direction of the normal force and the center of pressure should be known. After (Richards et al., 2008) the center pressure coordinates are calculated in the equation (2.44).

$$\begin{aligned} X_{CP} &= \frac{c}{4}\frac{90-|\alpha|}{90}\cos(\zeta) \\ X_{CP} &= \frac{c}{4}\frac{90-|\alpha|}{90}\sin(\zeta) \end{aligned} \tag{2.44}$$

where *c* is defined as the chord of the flat plate while ζ is the angle formed between the velocity and local x-axis of the plate Xp. After Richard et al. (2008) the expressions *c* and ζ are calculated in the equation (2.45).

$$\begin{aligned} \tan\zeta &= \frac{\tan\beta}{\frac{L}{l}} \\ c &= \frac{Ll}{L|\cos\beta|+l|\sin\beta|} \end{aligned} \tag{2.45}$$

While the particle displaces in the space, it rotates. This rotation is caused by a moment. The moment applied to the particle is divided into two: the static moment and the dynamic moment. The summation of both static and dynamic moment gives the total moment in equation (2.46).

$$\boldsymbol{M_t} = \boldsymbol{M_p} + \boldsymbol{M_d} \tag{2.46}$$

The static moment is introduced due to the shifting of the center of gravity from the center of pressure in most cases in the study like shown in figure 2.9. Thus, the static moment $\mathbf{M_p}$ is calculated in the equation (2.47) (Ignatowicz et al., 2019).

$$\boldsymbol{M_p} = \overrightarrow{C_p C_G} \times \boldsymbol{F} \tag{2.47}$$

F is the normal aerodynamic resultant force in the global frame of reference, C_p is the center of pressure and C_G center of gravity of the particle. The dynamic moment of the particle is due to the rotation of the particle in the space around the three axis Xp, Yp and Zp. The dynamic moment used, follows the one suggested by Ignatowicz et al. (2019) and calculated in the equation (2.48).

$$M_d = \frac{1}{2}\rho|V_{re}|^2 \begin{bmatrix} l^2 L C_{mrx} \\ L^2 l C_{mry} \\ 0 \end{bmatrix} \tag{2.48}$$

In the equation (2.48), C_{mrx}, C_{mry} and C_{mrz} stands for the dynamic moment coefficient components. The dynamic moment coefficient is calculated by the following equation (2.49) (Ignatowicz et al., 2019).

$$C_{mr} = \begin{bmatrix} sign(P) F_{DM}\left(\frac{|P|}{P_0}\right) \\ sign(Q) F_{DM}\left(\frac{|Q|}{Q_0}\right) \\ 0 \end{bmatrix} \tag{2.49}$$

where the expressions for P_0 and Q_0 stands for maximum angular velocity and it is calculated by the following equations (2.50) (Ignatowicz et al., 2019).

$$\begin{gathered} P_0 = 2(-1.25\frac{e}{l} + 0.516)\frac{|V_{re}|}{l} \\ Q_0 = 0.8\frac{|V_{re}|}{L} \end{gathered} \tag{2.50}$$

once the dynamic and static moments are known as well as the inertial matrix of the plate, the momentum equation (2.38) then could be solved.

2.3 Monte-Carlo Simulation

The Monte-Carlo approach is proposed to determine the zones where the particle has some probability of passage. Aircraft ice shedding is a complex phenomenon that creates random initial conditions for the trajectory calculation. The Monte-Carlo method enable to take into account the uncertainties of the initial conditions created by the shedding. The probability of passage in selected area behind the wing is obtained by multiple trajectory calculation. The main drawback of the approach is the number of trajectories needed for statistically relevant results, around 30,000 trajectories (Papadakis et al., 2007) if no shape is assumed for the probability distribution function. This would require a huge simulation time. Thus, a method that assumes the shape for the PDF is proposed to reduce the number of the trajectories necessary for this study.

The initial conditions that can be randomly varied for ice shedding are the size of the particle, the initial linear and angular velocity, the shed location and the ice piece orientation with respect to the three axis orientation of the global plane of reference. In this research, the initial data to be varied are the initial orientation and the initial velocity of the particle. The initial parameters are calculated randomly in MATLAB through random number generator. The ice particle is chosen to be a homogeneous rectangular flat plate.

The Monte-Carlo approach used in this study uses a variation of two parameters. The parameters to be varied are the initial velocity (Up, Vp, Wp) of the particle and the initial orientation angles (pitching, rolling, yawing). For the initial-rotation angle, the equation (2.51) is used (Ignatowicz et al., 2019):

$$\theta, \psi, \phi = (R - 0.5) \times Ri\,(180) \tag{2.51}$$

where, R is a random generator between 0 and 1, Ri is a MATLAB function from MATLAB toolbox to produce random integer numbers to alternate the angles between 0 and 180 degrees.

The 0.5 in the equation (2.51) stands for the alternation between -90 and +90. Note that this choice was used in Ignatowicz work and also used in this research. The three components of the initial velocity of the particle is obtained by equation (2.52) (Ignatowicz et al., 2019).

$$V_i = 0.7R \tag{2.52}$$

The combination of the initial variable parameters creates the initial conditions to start the trajectories simulation. Figure 2.10 show an example of the study domain. The solid body in this study is a wing of 5 (m) span possessing a NACA0012 airfoil at all section. The selection of a NACA0012 airfoil at all section of the wing is for validation with respect to the available experiments in the literature. The trajectories will cross a certain plan after the wing: the point of intersection between the plan and the trajectory is called footprint. Those footprints are collected at a plan situated at 6.5 (m) after the wing.

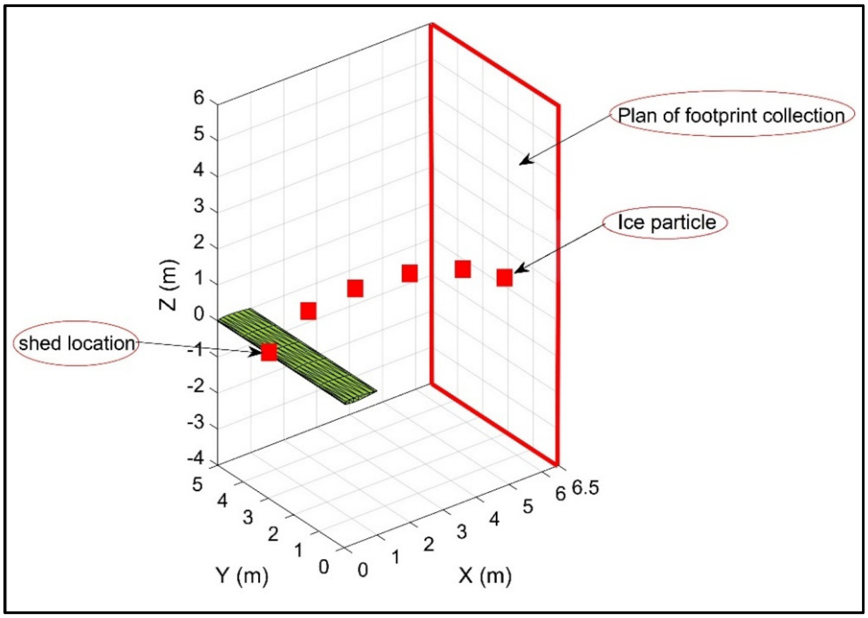

Figure 2.10 Illustration of the wing as well as the shed location and the plan where the footprints are collected.

The main problem facing this study is the huge number of trajectories to fulfill Monte-Carlo simulation for footprint map prediction. The suggested method in this research to predict correctly the footprint map is through a PDF prediction. The calculations of the PDFs will be explained in the next section.

2.4 PDFs estimator

To predict a PDF a hypothesis should be made. This study is dealing with 3D PDF because the footprints are collected in a plan possessing *y* and *z* coordinates. Thus, it is complicated to assume a shape for the 3D PDF. That's why, a projections of the 3D distribution P (Y, Z) along the Z-axis called P(Z) and along the Y-axis called P(Y) are used. The projections are done to make the probabilities easier to analyze and predict. Since the trajectories obtained are either on the upper or lower side of the wing, the probability along P(Z) could be assumed to be a binormal distribution while the projection along P(Y) could be assumed to be normal distribution. This hypothesis is inspired by Suares (2005) probability distribution results, since most of the shapes of the bins distributions that he got tend to look like normal and binormal distribution. Dealing with the footprint data will be done using the function *ksdensity* of MATLAB toolbox. This function is called Kernel Smoothing PDF (KSPDF)(Bowman & Azzalini, 1997). It estimates the probability distribution shape after drawing the data as histogram. The kernel density estimator for the PDF shape of any footprint data for any real value of *x* could be estimated as, equation (2.53).

$$f_h(x) = \frac{1}{Nh}\sum_{i=1}^{N} K\frac{(x - x_i)}{h} \tag{2.53}$$

where, *N* is the number of footprints, *h* is the bandwidth coefficient and *K* (*x*) is the kernel smoothing function. The kernel estimator for the cumulative distribution function CDF, for any real values of *x* (*x* represents the footprints coordinates) is given by the equation (2.54).

$$F_h(x) = \frac{1}{n}\sum_{i=1}^{n} G\frac{(x - x_i)}{h}$$

$$G(x) = \int_{-\infty}^{x} K(t)\,dt \tag{2.54}$$

The shape of the distribution is obtained after drawing the data as histogram (the choice of the bins is done automatically by the MATLAB function *Distributionfitter*). To know the exact shape of the PDF, the function is now fitted into an application called *DistributionFitter* in MATLAB toolbox. It allows to fit any distribution function (normal, lognormal, exponential, etc..) with the shape obtained from KSPDF. This fitter works the same way as the function *fitdist* (Bowman & Azzalini, 1997) but with user interface. After the normal shape has been fitted, the mean and variance are estimated. Furthermore, a test will be done to P(Z) and P(Y) called Kolmogorov-Smirnov test (K-S test) for normality through the continuous cumulative distribution function (CDF) (Massey Jr, 1951). After the PDF is verified for normality, the mean and variance for each PDF are compared. The test statistic is performed by computing the maximum absolute difference between the empirical CDF (ECDF) (from current P(Y) or P(Z)) and the hypothesized CDF (HCDF)(standard normal CDF) (Massey Jr, 1951) equation (2.55).

$$Pr = [\max|S_N(x) - F_0(x)| > d_\lambda(N)] = \lambda \tag{2.55}$$

where λ is the significance level taken from the table of data from Massey Jr (1951) equal to 0.05. $S_N(x) = k/N$ is the observed cumulative step-function (HCDF) where *k* is the number of observations less than or equal to *x*. The sampling distribution $d_\lambda(N)$ is equal to $\frac{1.36}{\sqrt{N}}$ as the number of footprints *N* is more than 35. This choice is based on the paper recommended practices of Massey Jr, (1951). The criterion to find the minimal number of trajectories is by computing the error between the means of the PDFs for every set of trajectories simulated. The error criteria is ε = 0.01. This criterion is also applied for the variance of the PDFs.

2.5 Code implementation

This section illustrates the methodology implementation through MATLAB. Figure 2.11 shows the trajectory code algorithm in MATLAB. The 3DPM computes and provides the flow field solution for example source and doublet (equation (2.24)). Those two strengths are used to calculate the velocity anywhere in the flow field (equation (2.32)) necessary to the Newton's second law of motion, implemented into the trajectory code. One trajectory is obtained from the release of the ice particle in the space for one second with a time step of 0.001 second. The initial shed location is fixed. The initial orientation and velocity of the particle are calculated randomly and provided to the trajectory code as inputs. The Monte-Carlo simulation is based on an repetitive process by computing several trajectories (random trajectories sampling with every trajectory is calculated independently). The functions were written to separate the particles that flow downstream the wing, from the particles which stroke the wing surface. The footprints coordinates (*y, z*) at the plan of interest are collected and stored in matrices for further studies. The last function is for the PDFs estimation.

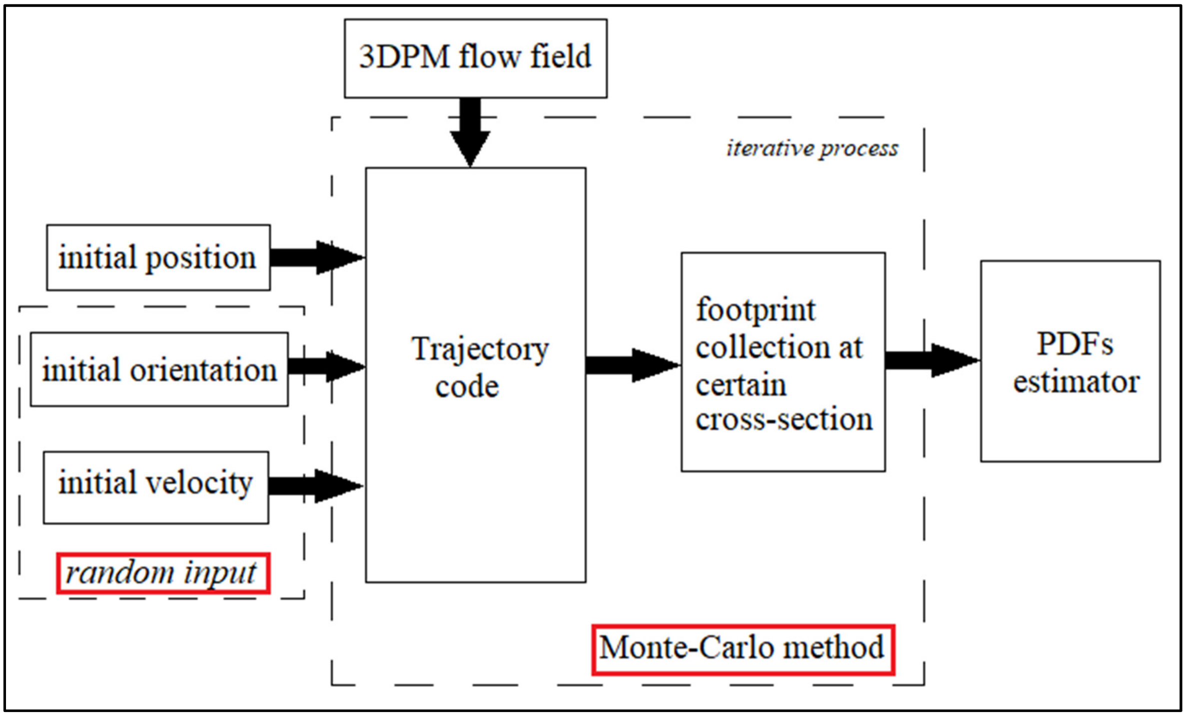

Figure 2.11 Method computation for Monte-Carlo simulation.

CHAPTER 3

RESULTS AND DISCUSSION

This chapter holds two sections. First will be the validation and verification of the results, which holds the verification of the flow field correction by closing the wing tip of the geometry used, and the trajectories verifications from both 3DPM and CFD. A comparison of the pressure coefficient with 2D and 3D infinite wing is being illustrated. Secondly, a Monte-Carlo method is used to predict a footprint map at the plan of interest after the wing. Also, the PDFs predictions based on the hypothesis in the methodology is verified for each case. Also, calculations is carried out to check the minimal number of trajectories to fulfill Monte-Carlo approach.

3.1 Validation and verification

3.1.1 Wing tip closure effect

As mentioned in the methodology, the closure of the wing tip will affect the overall flow field around the wing. The geometry provided in this program can be any wing based on any airfoil. The solid body in this study is a wing based on NACA0012 airfoil with open wing tip. An improvement to the initial program has been implemented to close the wing tip, aiming to correct the flow at the tip of the wing and then the overall flow.

The wing is discretized spanwise and chordwise by different numbers of panels. 18 panels are used chordwise and five panels do the discretization spanwise. The flow is incompressible with a velocity of 1 m/s, the span is 10 m, the chord length is 1 m, thus giving an aspect ratio of 10. The lift and pressure coefficient are calculated only at the collocation point. As for the open source software XFLR5 v6.43 (Deperrois, 2009) used to generate reference results, the same mesh is used with the same flow parameters.

Figure 3.1 illustrates the lift force coefficient versus the angle of attack. It represents a comparison of the lift coefficient from the open source software XFLR5 with the one obtained by the 3DPM with and without wing tip patch. The advantage of using XFLR5 software is that it solves the non-viscous incompressible flow using a 3D panel method, similar to the one used in our code. Clearly after closing the wing tip, the lift coefficient shows an agreement with 3.24% of error with XFLR5 (possess a 3DPM with a closed wingtip patch).

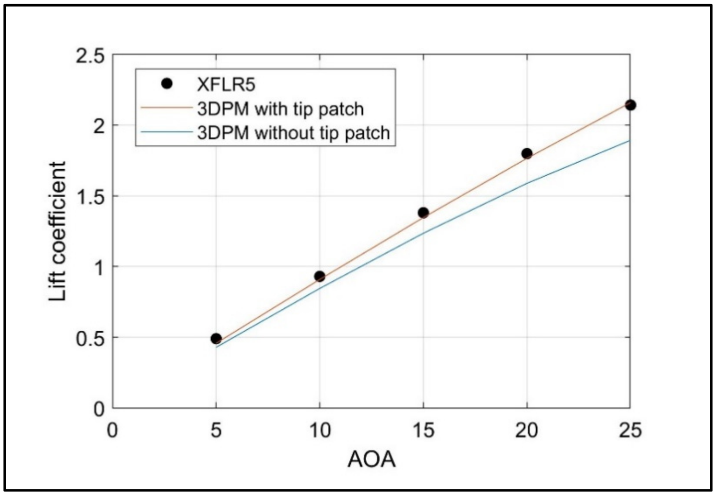

Figure 3.1 Total lift coefficient comparison between the software XFLR5 and panel method code for flow correction

Figure 3.2 shows the pressure coefficient with respect to the chord length. The pressure coefficient obtained from 3DPM is compared against the one obtained from the software XFLR5. The pressure coefficient is calculated at the root section. The evolution of the pressure coefficient with respect to the mesh used is obtained. The three different meshes having 18, 26 and 36 panels chordwise and 5 panels spanwise. The spacing between the nodes is not uniform: more node existed near the leading edge and the trailing edge. In Figure 3.2, the 3D panel code and the software XFLR5 had an agreement with a maximum Cp difference error of 5.44 %. These differences are due to different geometrical discretization at the wing leading edge. These differences do not affect the trajectories calculation as shown in the next verifications.

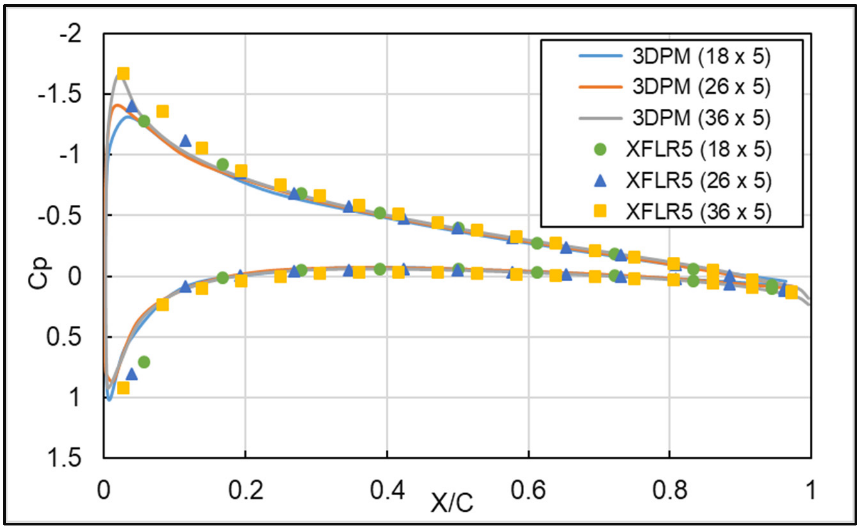

Figure 3.2 Comparison between the current panel code and the software XFLR5 for the pressure coefficient at AOA = 5° and different numbers of panels.

The wing tip closure have corrected the flow field around the wing. This correction is verified by comparing the lift coefficient and pressure coefficient with the 3DPM code and XFLR5. The next section shows a validation of the flow against the experimental as well as a comparison of the trajectories using different flow fields.

3.1.2 Trajectories verification

The trajectories calculations are based on a 3DPM flow field solution. The flow field first should be validated. This test case is a comparison between experimental pressure coefficients around a 2D NACA0012 airfoil and an infinite wing based on the same airfoil at all sections. The concept of infinite wing can be obtained by setting a high aspect ratio, because the 3DPM with closed wing tip used in this study can only model a finite wing. That’s why, a wingspan of 100 m with aspect ratio equal to 100 can be assumed to have a close behavior as the one of an infinite wing. The 2D results was obtained from the experimental wind tunnel test obtained by NASA (Harris, 1981). The pressure coefficient is extracted from the 3DPM code solver, at the middle section of the wing and compared with 2D experimental results. The flow velocity is 10 m/s (the velocity is taken 10 m/s to match the initial conditions of the experiment). The results show an agreement between the 2D and 3D case with a maximum error of 0.8 %, even if the 3DPM model does not include viscous effects. The AOA = 5.86° corresponds to the experimental conditions.

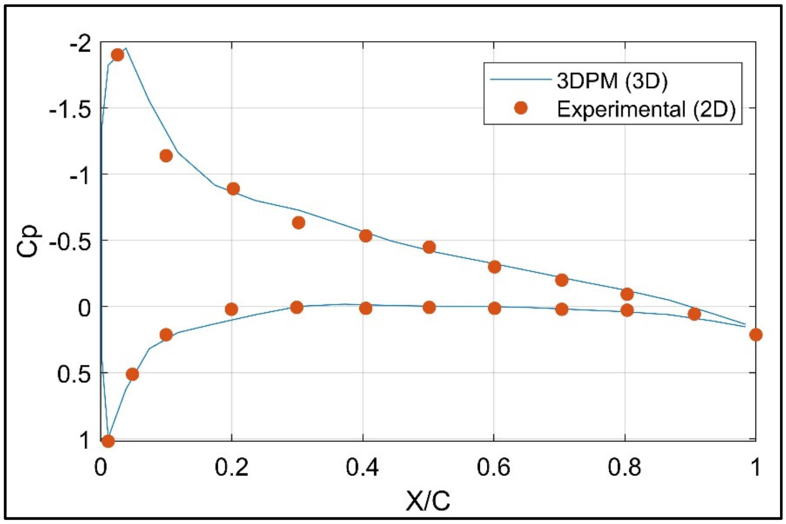

Figure 3.3 Pressure coefficient comparison between 3DPM code and experimental results

Figure 3.4 shows a comparison of the pressure coefficient at the middle section of the wing. The first result is obtained by the 3DPM code solver. The geometry (18 x 5) used is a 1 m chord by 1 m span with free stream velocity of 1 m/s with an AOA of 0 degree. The second result is from a CFD mesh which has been obtained from (Tagawa, Morency, & Beaugendre, 2018). The CFD solution is performed considering Euler's equation. The CFD solution is obtained using the open source SU2 software version 6.1.0 (Economon, Palacios, Copeland, Lukaczyk, & Alonso, 2015). The solid body is a wing of 1 m chord wing with 1 m span, 0 degrees angle of attack and a free stream velocity of 1 m/s. The third results is obtained by the open software XFLR5 using the 3DPM implemented inside. The geometry and the input parameters used in the XFLR5 are the same used in the 3DPM code solver. The compared results show an agreement of 0.5% of maximum error.

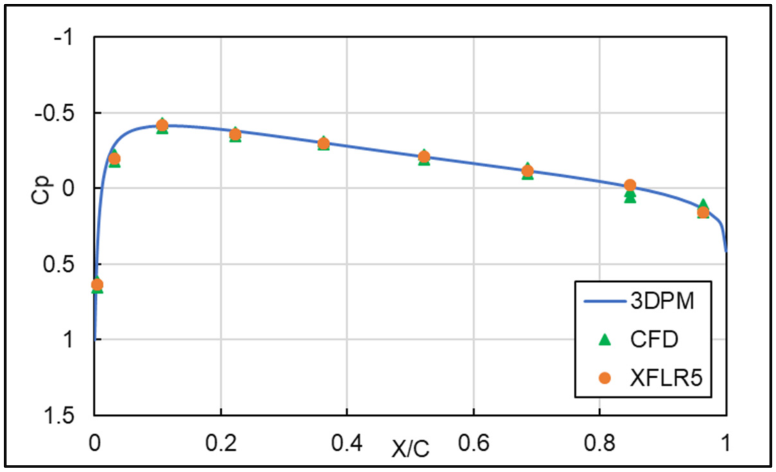

Figure 3.4 Pressure coefficient comparison at AOA = 0°.

After verifying the pressure coefficient, the flow field around the wing using 3DPM could be used for further calculations. The verification of the farfield velocities is done by a comparison between two trajectories from two different flow field : CFD and 3DPM flow field. The flow field obtained from the 3DPM code solver described in the previous test case is used. In this test case, the particle is chosen to be a flat plate with rectangular shape. The initial angle of rotation of the ice block is 90 degrees. The dimensions of the piece are 0.2122 x 0.1601 x 0.002 m, the density of the particle 170 kg/m^3 and the air density is 1 kg/m^3. The shed location is at the leading edge at 0.5 m from the root section. Figure 3.5 and Figure 3.6 shows an XZ view and YZ view of a trajectory respectively. The comparison presents an agreement with maximum 4.14% of error on X-direction while it agrees well in the YZ direction.

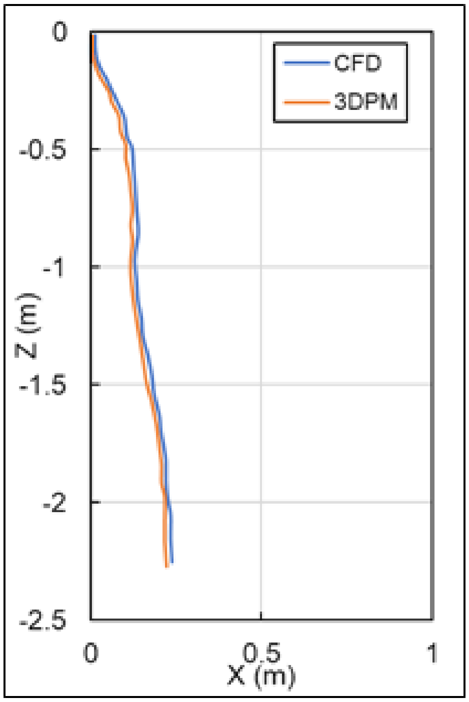

Figure 3.5 XZ view of the trajectories.

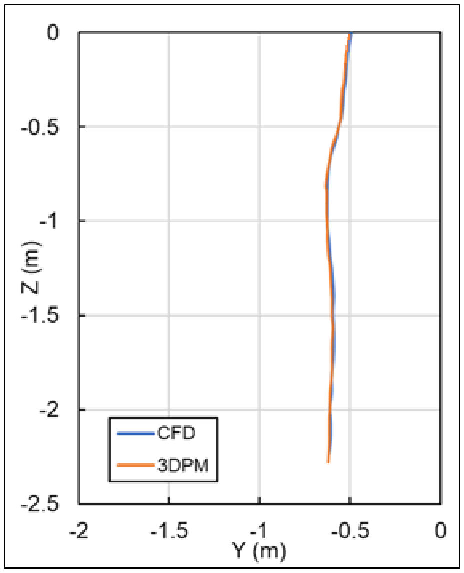

Figure 3.6 YZ view of the trajectories.

Moreover, an additional verification is done against Suares (2005) results. Since Suares performed a 2D probabilistic study on the trajectory's footprint along the z-axis, the projection to z-axis of the footprint of the particle obtained from the 3DPM could be compared to Suares work. Suares specified that he simulated 60,000 trajectories in the beginning of his methodology but didn’t specified the number of trajectories simulated for this test case neither the number of collected footprints at z-axis. The present code simulated 500 trajectories. The probability map of Suares is done with the following conditions: 3-DOF (two translational motion and one rotational motion (pitching)) in 2D airfoil (NACA23012) flow field, the flat plat is squared with 0.3(ft) length and 0.025(ft) of thickness with randomness of the initial angle of rotation and initial velocity of the particle. Note that Suares used a CFD solution while this study uses the 3DPM flow field solution.

Table 3.1 Initial conditions for Suares simulations

Initial parameters	
Flow field velocity (m/s)	113
Flat plate (ft^3)	0.3 × 0.3 × 0.025
AOA (°)	4
Plan of footprint collection	2 × Chord

The results are shown in the figure 3.7. The results show the probability distribution at the z-axis where the footprints are collected. The tendency of the two distributions is similar at z-axis where the maximum of the bins for the two cases is between 2.75 and 3.25 ft. Exact comparison of distribution is impossible to obtain. This happens because the code of Suares used correlations not specified well in his paper.

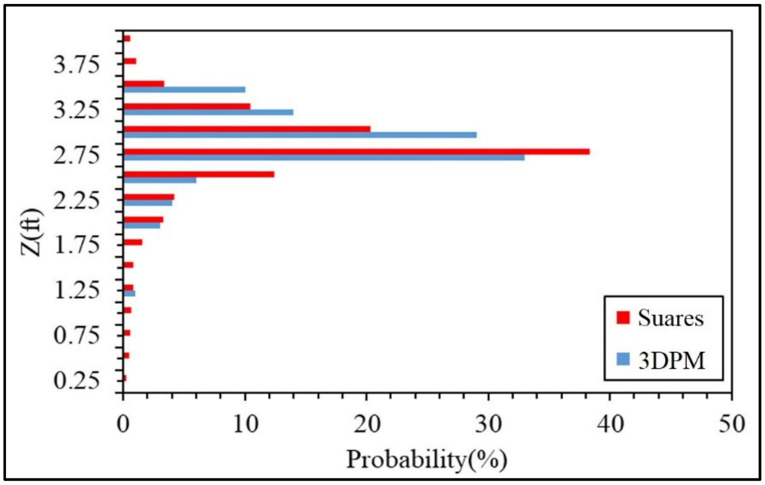

Figure 3.7 Probability distribution of the trajectories at x = 2c plan behind the wing at AOA = 4° with NACA23012 airfoil.

The previous section presented a validation of the flow field, and a verification of the trajectory code against the literature. The 3DPM in MATLAB code was verified against the open source software XFLR5. Also, one trajectory is compared using both 3DPM and CFD. Moreover, a footprint probability distribution along the z-axis was obtained from the 3DPM flow field and was compared to the literature.

3.2 Monte-Carlo simulation

Based on the validation and the verification of the flow field and the trajectory code done in the previous section, a parametric study of the trajectory's footprint using the Monte-Carlo method will be presented. The footprints of the ice trajectories at the plan situated at 6.5 m downstream the flow are depicted. Each section will show the ice shedding at the plan of collection upside and downside the wing. The ice particles are assumed to have a fixed shape in all the forgoing simulations. The flat plate is rectangular and has a dimension of 0.2122 m × 0.1061 m × 0.002 m, the mass of the plate is 7.6 g uniformly distributed. The shed location is at 3 m from the wing root section at the leading edge. It was assumed that the shed location is in front of the wing leading edge by 0.01 m to avoid collision of the particle with the leading edge.

The wing used in this test case possesses a NACA0012 airfoil at all sections. The wing and flow field characteristics are illustrated in the next table. The panel discretization is chosen because it fasten the trajectory's computation and doesn't impact the trajectory's result.

Table 3.2 Wing and flow field characteristics for Monte-Carlo method

Wing characteristics			**Flow field characteristics**	
Span (m)	5		Free stream velocity (m/s)	113
Panels discretization	18 × 5		Altitude (ft)	15 000
Aspect ratio	5		Air density (kg/m^3)	0.77
Chord length (m)	1		Gravitational acceleration (m/s^2)	9.671

A good prediction of the footprint map requires simulating a minimal number of trajectories to fulfill the Monte-Carlo method. The process of estimating the minimal number of trajectories lies on good PDFs estimation by assuming the shape of the PDFs. Thus, the hypothesis assumed in the methodology section (P(Z) binormal and P(Y) normal) is verified by running two test cases while varying two parameters and fixing one parameter. The first test case will consider a fix sweep angle, and two parameters varying: the angle of attack and the number of trajectories. The second test case will consider a fixed angle of attack while varying the sweep angle and the number of trajectories.

3.2.1 Effect of angle of attack

This section will compare the footprint map at the plan of interest at AOA = 0°, AOA = 5°, AOA = 10° and AOA = 13°. The sweepback angle (SBA) is fixed at zero degrees. As mentioned in the methodology section only the angle of rotation and the initial velocity of the particle are changing randomly. In this section, two main parameters will be changing: the angle of attack and the number of trajectories. Firstly, the angle of attack is changed while fixing the number of trajectories to show the effect of the angle of attack on the footprint map. Secondly, the angle of attack is fixed at 5 degrees while varying the number of trajectories to check the effect of number of trajectories on the footprint map.

Figure 3.8 shows the variation of the footprint map with respect to the angle of attack variation. For this study 200 trajectories are simulated. The wing is represented in red color. The figure shows that the footprints are upside and downside of the wing. When the angle of attack increases, the footprints shift upward. The number of footprints is higher in quantity on the upside of the wing than the downside when the AOA increases.

In the Figure 3.9, the AOA is fixed at 5 degrees and the sweepback angle (SBA) also remains fixed at zero degrees. The number of trajectories simulated varies between 50, 200, 500 and 1000 trajectories. The case of 5000 trajectories is also simulated and taken into account in the results, but it is not shown in figure 3.10 because the results of 5000 trajectories are similar to the results of 1000 trajectories and are shown in the ANNEX I. By increasing the number of trajectories simulated, the footprint map will be denser. Thus, the areas where the footprint could have risk of passage are determined in the plan of interest. With 50 trajectories, it is impossible to see a region of high possibility of passage upside and downside the wing. By increasing the number of simulated trajectories to 200, it is seen that most of the footprints are between z = -1 m and z = -2 m, in the downside of the wing and between z = 2 m and z = 3 m in the upside of the wing which is substantiate by the 500 and 1000 trajectories. The footprint map shows a small change with the variation of the number of trajectories. To prove this, a study is done using the PDF in later section.

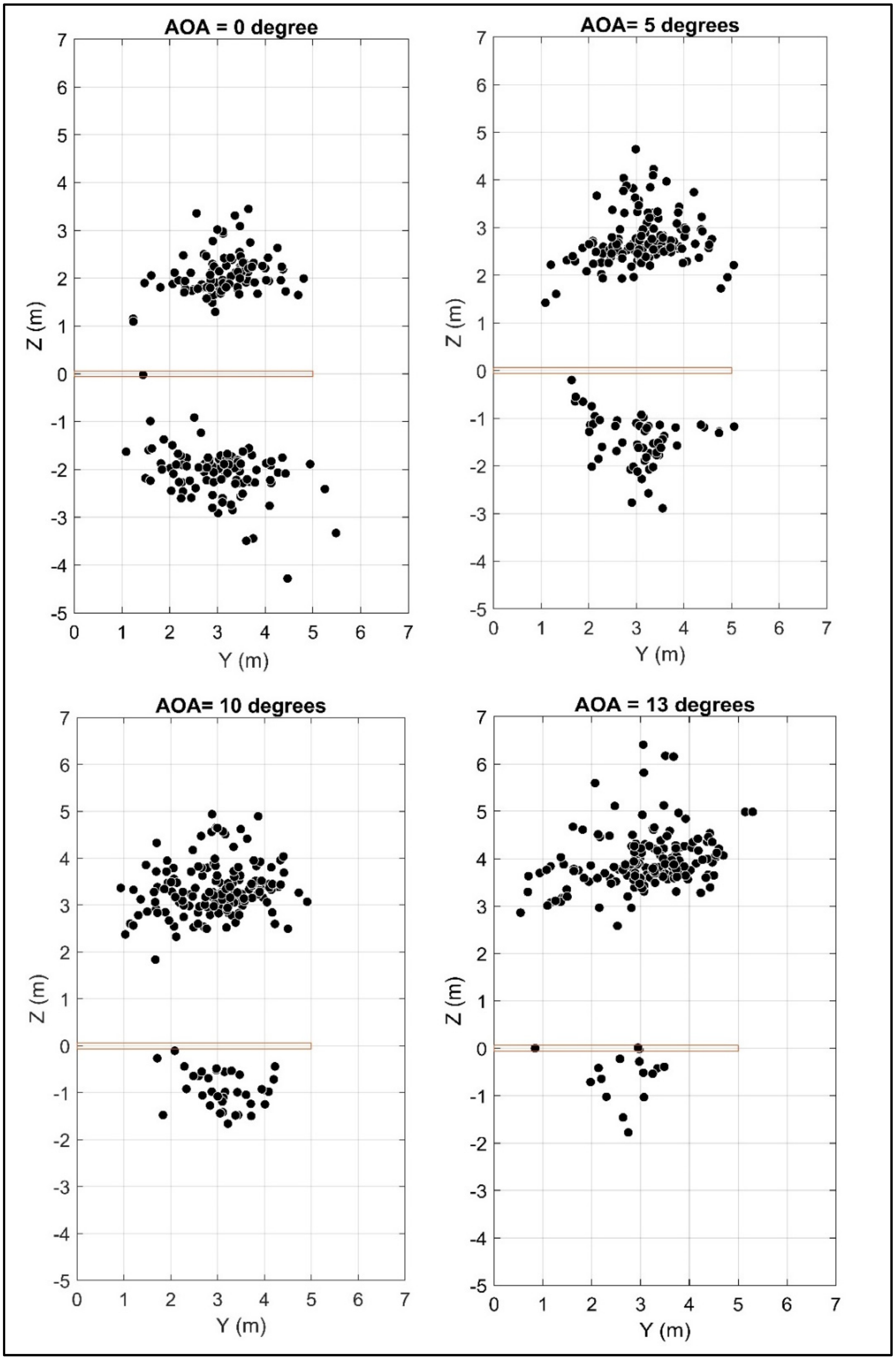

Figure 3.8 Variation of trajectories footprint with respect to the angle of attack SBA = 0°, number of trajectories = 200.

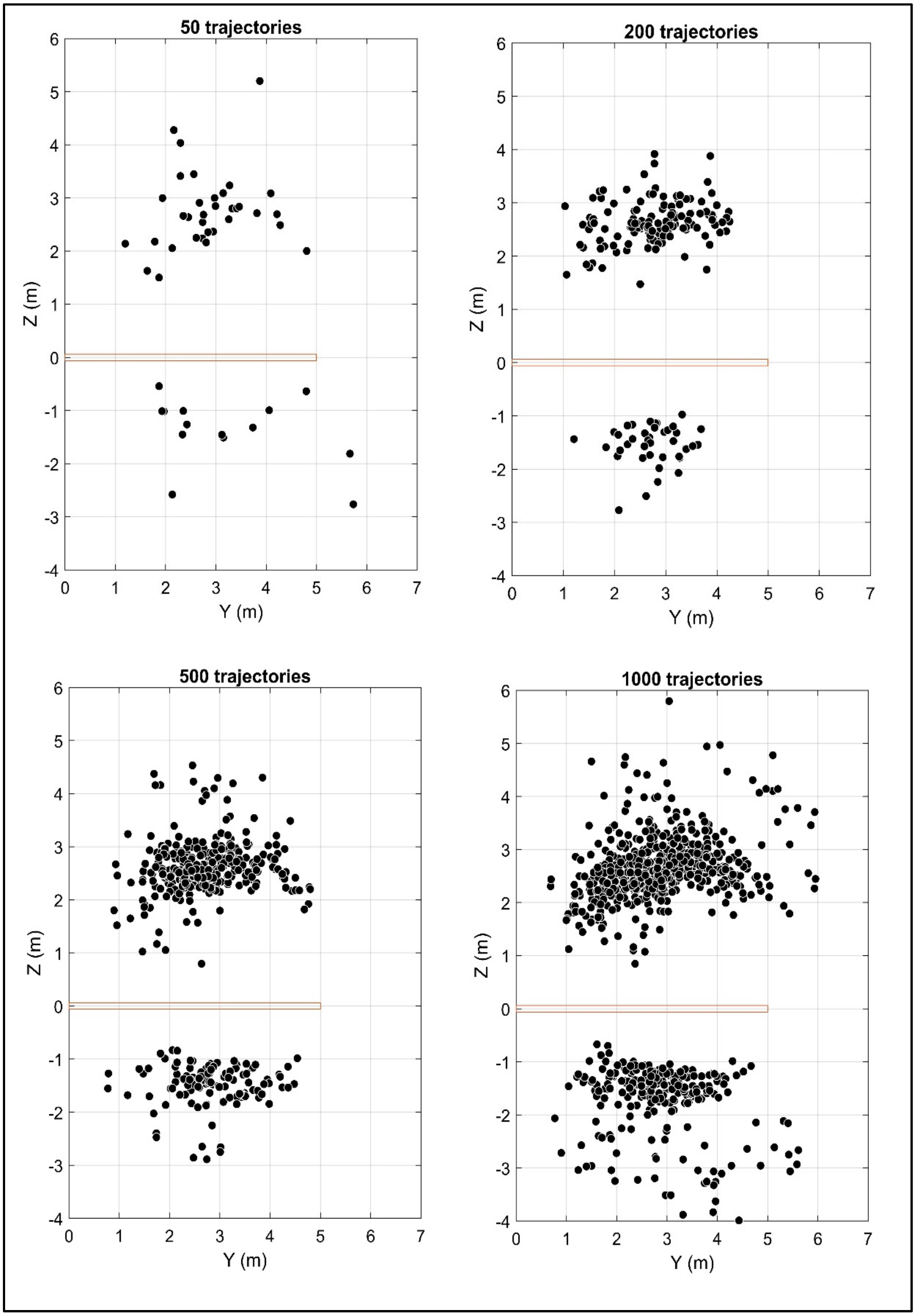

Figure 3.9 Variation of number of trajectories footprint, AOA=5°, SBA=0°.

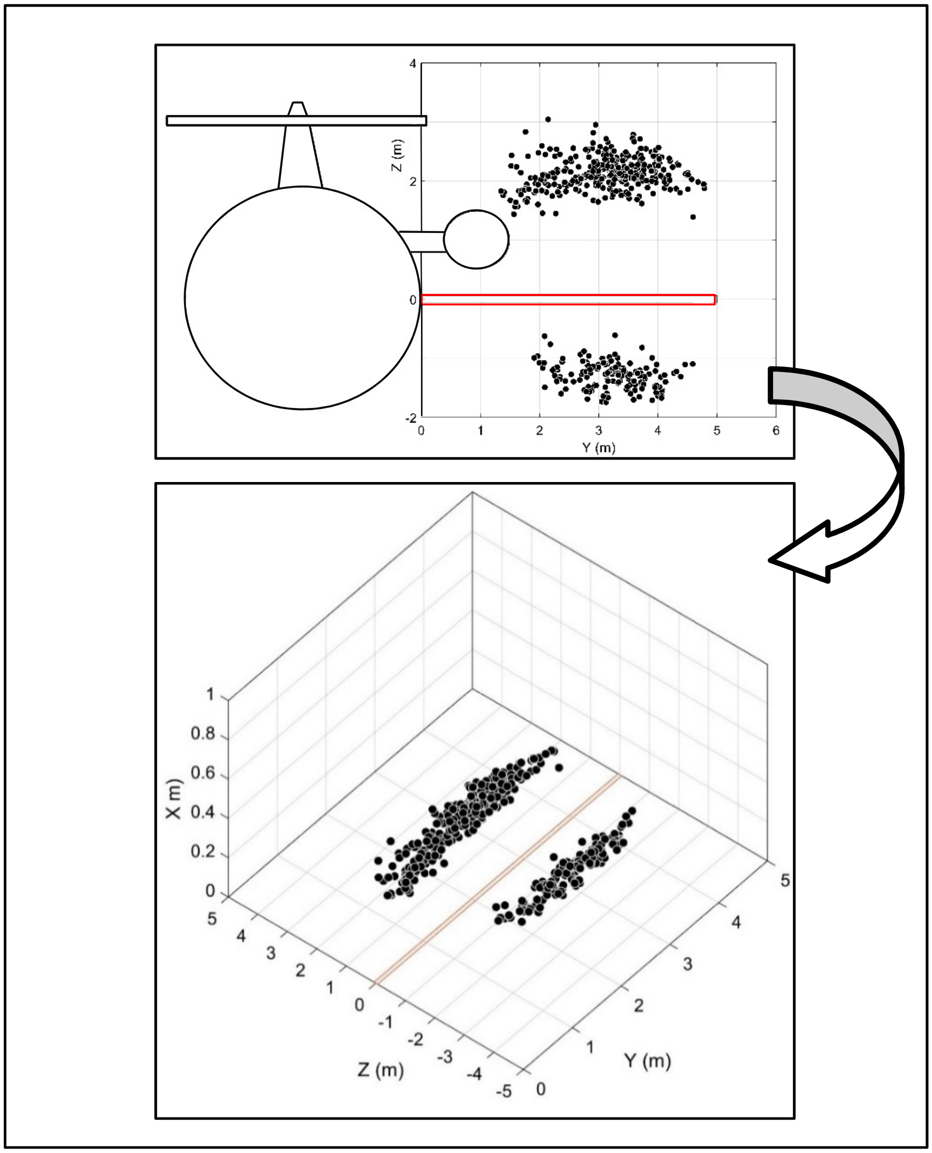

Figure 3.10 Rotation of the plan

Figure 3.11 shows the 3D probability distribution P (Y, Z) for 500 trajectories. The reason for choosing 500 trajectories is to pick a case to show the 3D PDF of the footprints of the trajectories at the plan of interest. This probability distribution was projected along the z-axis and the y-axis of the aircraft to simplify the task of the PDF comparison. This distribution was obtained by writing a MATLAB function to depict the 3D view of P (Y, Z). The projection along z-axis is called P(Z) and the one along y-axis is called P(Y). Figure 3.10 shows the view rotation. This is done to clarify the plot of the figure 3.11.

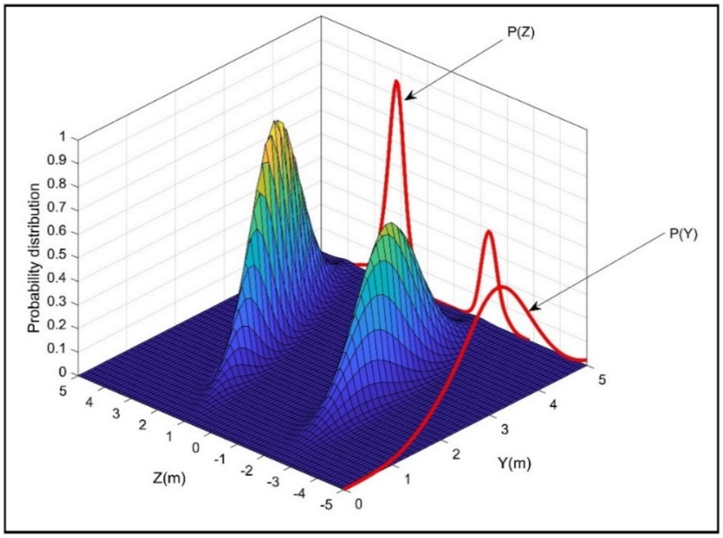

Figure 3.11 3D probability distribution of the footprint trajectories for 500 trajectories at AOA = 5° and SBA = 0°.

Figure 3.12 represents the projection P(Z) along z-axis. In this case, the probability distribution was plotted for different number of trajectory's footprint. The number of trajectories simulated was 50, 200, 500, 1000 and 5000 trajectories. As shown, the probability distribution takes the shape of a binormal distribution function. The data where the footprints are downside in the negative side of the z-axis is called function (1) and the data where the footprints are on the upside of the wing or in the positive side of the z-axis is called function (2). The function P(Z) is assumed to be binormal. Firstly, the shape of the PDF is drawn by means of MATLAB toolbox in a fitter called *DistributionFitter* using the KSPDF equation. After the KS test is applied to the PDF for normality.

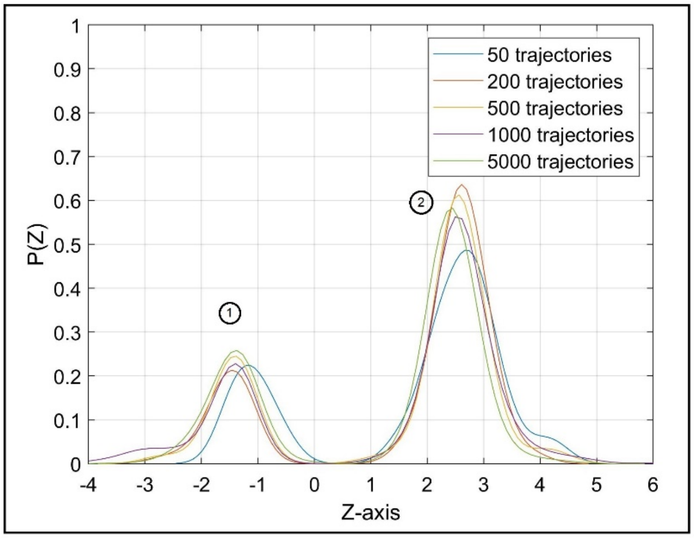

Figure 3.12 Probability distribution of the trajectory's footprint with respect to the z-axis.

Figure 3.13 shows the comparison between the empirical CDF (ECDF) and hypothesized CDF (HCDF) for P(Z). The set error between the two curves lies on the criteria of the KS test with a maximum error of 5%. After computing the error for the first and second function at 500 trajectories, the maximum error was found to be 4.52%. The maximum error for the 1000 trajectories was computed to be 4.18% between the ECDF and HCDF.

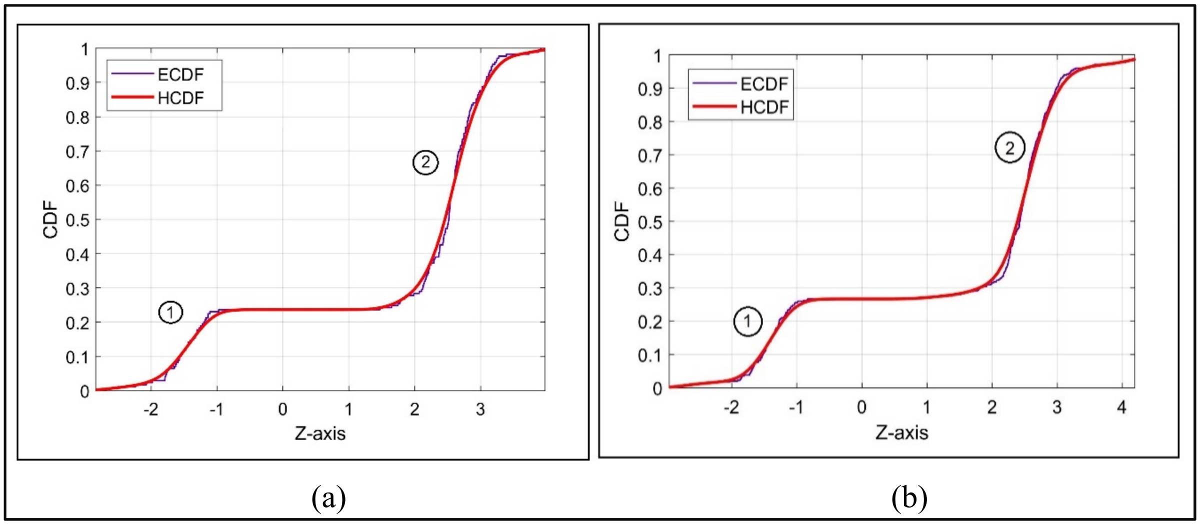

(a) (b)

Figure 3.13 Cumulative probability distribution for P(Z) for 500 trajectories (a) and 1000 trajectories (b).

After the binormal assumption is approved for P(Z) at 500 and 1000 trajectories, the minimal number of trajectories needed to fulfill the Monte-Carlo approach should be calculated. The mean and variance for every case are calculated because they are the key characteristics from which the minimal number of trajectories will be found. As mentioned in the methodology, the criteria is set by computing an error of ε = 0.01 for both mean and variance. In other words, the mean and variance doesn't change with the increase of number of trajectories up to a precision of 0.01.

Figure 3.14 shows the mean for P(Z) (1). At 50 trajectories, mean 1 was around -1.1. When the number of trajectories simulated increases, the mean 1 decreases until it reaches a value of -1.612 at 500 trajectories, -1.624 at 1000 and -1.619 for 5000 trajectories. The mean (2) took the same behavior as mean (1) like expected. At 50 trajectories the mean (2) was 2.68. When the number of trajectories simulated increases the mean decreases until it reaches a value of 2.615 at 500 trajectories, 2.631 at 1000 trajectories and 2.627 at 5000 trajectories.

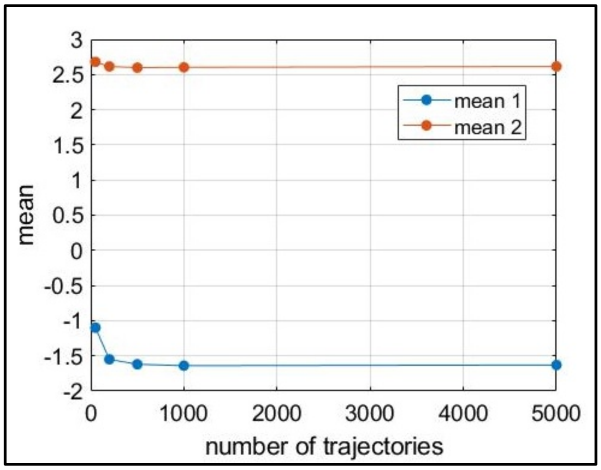

Figure 3.14 Mean variation vs number of trajectories for P(Z).

Figure 3.15 shows the variance for P(Z) (1). At 50 trajectories, variance 1 was around 0.105. When the number of trajectories simulated increases, variance 1 increases until it reaches a value of 0.1523 at 500 trajectories, 0.1532 at 1000 trajectories and 0.1545 at 5000 trajectories. The variance (2) also varied with the number of trajectories simulated. At 50 trajectories the variance (2) was 0.3512. When the number of trajectories increases the variance decreases to 0.2842 at 200 trajectories, 0.2813 at 500 trajectories, 0.2804 at 1000 trajectories and 0.282 at 5000 trajectories.

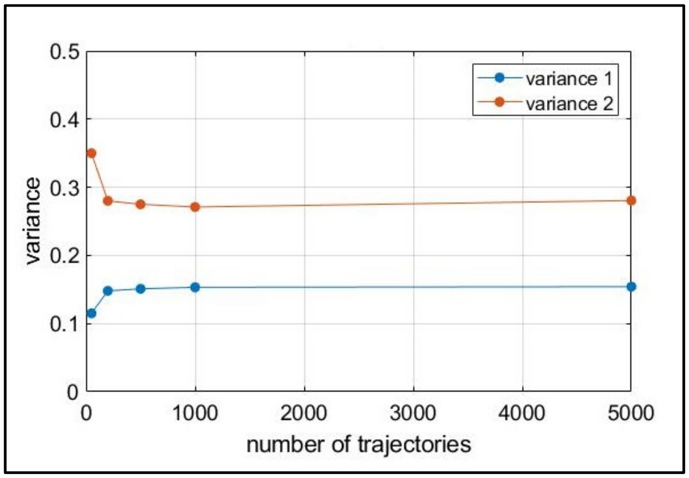

Figure 3.15 Variance variation vs number of trajectories for P(Z)

The mean and variance reach a point where it doesn't significantly change between 500 and 1000 (error = 0.001). This point is after 500 trajectories, which is the minimal number to predict an acceptable PDFs and thus a footprint map. Predicting just the shape of P(Z) is not enough. Thus, another study of the footprint data along the y-axis (spanwise) should be done.

Now the same distribution P (Y, Z) is projected along the Y-axis. The shape of probability distribution P (Y) was plotted for different number of footprint in Figure 3.16. The same number of trajectories simulated before is also used for this case: 50, 200, 500, 1000 and 5000 trajectories. As shown the probability distribution prediction takes the form of a normal distribution function. This assumption is proved by the same KS test mentioned in the methodology.

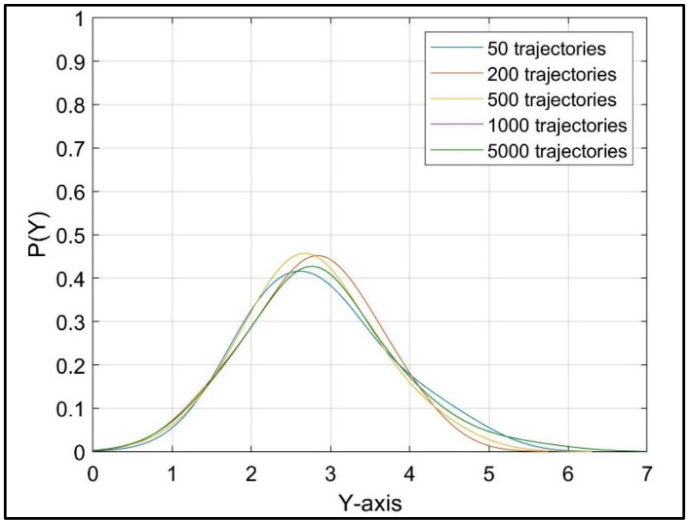

Figure 3.16 Probability distribution of the trajectory's footprint with respect to the y-axis.

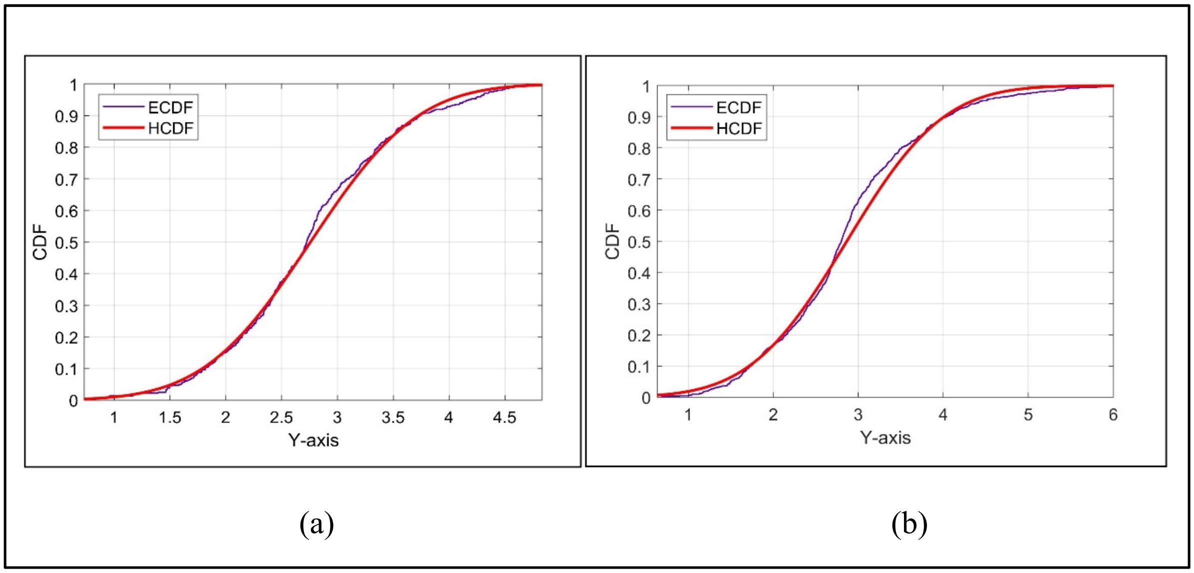

Figure 3.17 Cumulative distribution function for P(Y) for 500 (a) and 1000 (b) trajectories.

Figure 3.17 shows the comparison between the empirical CDF (ECDF) and hypothesized CDF (HCDF) for P(Y). The set error between the two curves lies on the criteria of the KS test with the highest error of 5%. After computing the error for the first and second function at 500 trajectories, the maximum error at y = 3 was found to be 3.21%. The maximum error computed for the 1000 trajectories is 3.95% between the ECDF and HCDF.

The mean and variance with respect to the number of trajectories for the normal distribution function P(Y) are shown on Figure 3.18 and Figure 3.19 respectively. In Figure 3.18, the mean at 50 trajectories is 2.851. When the number of trajectories simulated increases, the mean decreases until it reaches a value of 2.765 at 500 trajectories, 2.752 at 1000 trajectories and 2.755 at 5000 trajectories. In Figure 3.19, the variance for P(Y) with respect to the number of trajectories is shown. At 50 trajectories, the variance was around 0.704. When the number of trajectories simulated increases, variance decreases then increases until it reaches a value of 0.572 at 500 trajectories 0.581 at 1000 trajectories and 0.589 at 5000 trajectories.

.

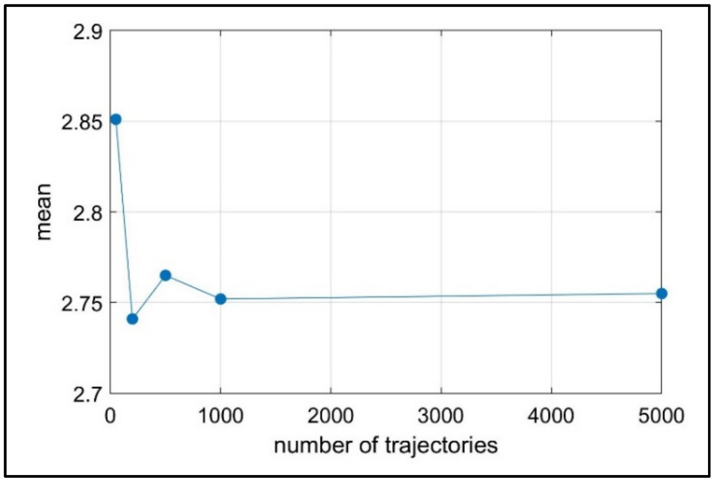

Figure 3.18 Mean variation vs number of trajectories for P(Y).

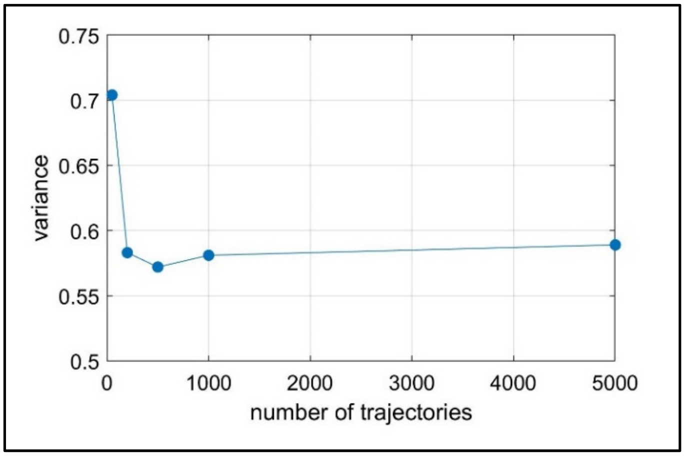

Figure 3.19 Variance variation vs number of trajectories for P(Y).

The study of the mean and variance at P(Z) shows that the mean and variance do not change significantly after 500 trajectories for both functions respecting the 0.01 significance error criteria. Moreover, the mean and variance for P(Y) also do not change significantly after 500 trajectories. Thus, the probability distribution P (Y, Z) is not changing after 500 trajectories which means that 500 trajectories is the minimal number at which the Monte-Carlo method could be fulfilled for this research. The next step is to check the effect of the variation of the sweepback angle on the trajectory's footprint map.

3.2.2 Effect of sweepback angle

This section uses the same wing and flow field characteristics simulated in the previous section. A comparison of the footprint map distribution will be done but this time by changing the sweepback angle (SBA). In this section, the changing parameters are the sweepback angle and the number of trajectories. The chosen sweepback angles are SBA = 0°, SBA = 15°, SBA = 30° and SBA = 45°. The footprint maps are obtained and illustrated in this section.

Figure 3.20 shows the variation of the footprint map with respect to sweepback angle. For this study 500 trajectories are simulated. The wing is represented in red color with 5 m of span. At SBA = 0 and 15 degrees, the footprints downside the wing are between z = -2 m and z = -1 m while the footprints at the upside of the wing are concentrated between z = 2 m and z = 3 m. At SBA = 30 degrees, the footprints downside the wing, most of them lies between z = -1.75 m and -1 m while the footprints upside the wing lies between z = 1.75 m and z = 2.5 m. Finally, at SBA = 45 degrees, most of the footprints downside the wing, are between z = -1.5 m and -1 m while the footprints upside the wing are mostly between z = 1.25 m and z = 2 m. When the sweepback angle changes from 0 to 45 degrees, the footprint map becomes less noisy. This happens because the particles lose part of the vertical velocity and gain a tangential velocity Vy by the effect of sweepback angle (division of the velocity components).

In the previous section, the sweepback angle was fixed at 0 degree while varying the angle of attack. In the Figure 3.21, the sweepback angle is fixed at 30 degrees and the number of trajectories simulated varies between 50, 200, 500 and 1000 trajectories. Also, 5000 trajectories are simulated, and the results are not shown in this section but shown in the ANNEX I. The region of high probability of passage upside and downside the wing is not well attainable in the 50 trajectories case. By increasing the number of simulated trajectories to 200, it is seen that most of the footprints are between z = -1.75 m and z = -2.5 m, in the downside of the wing and between z = 1.75 m and z = 2.5 m in the upside of the wing which is substantiate by the 500, 1000 and 5000 trajectories. The footprint map shows a small significant change with the variation of the number of trajectories. To prove this, a study is done using the probability distribution function (PDF) in later in this section.

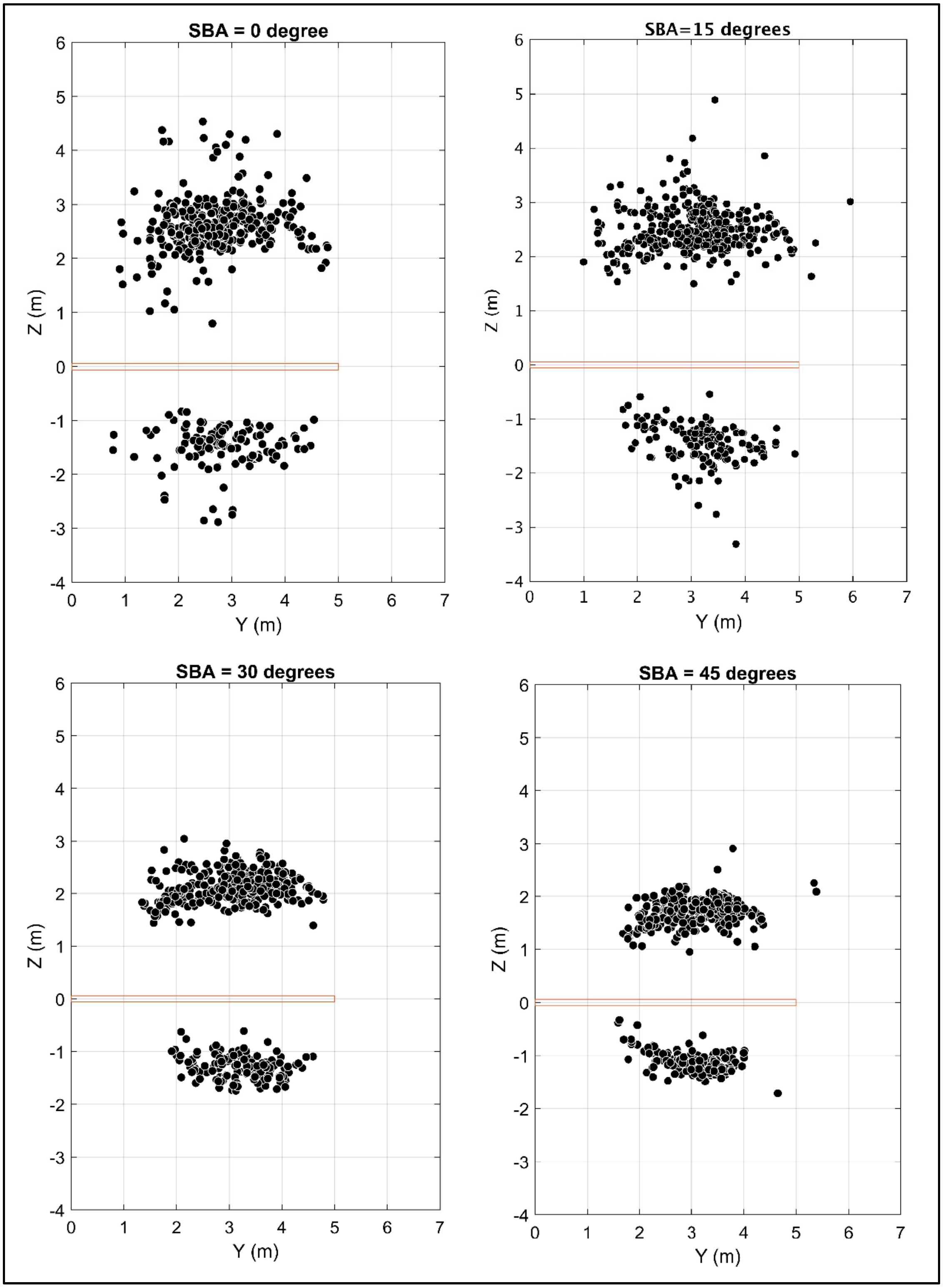

Figure 3.20 Variation of trajectories footprint with respect to the sweepback angle at plan = 6.5 m at AOA = 5°.

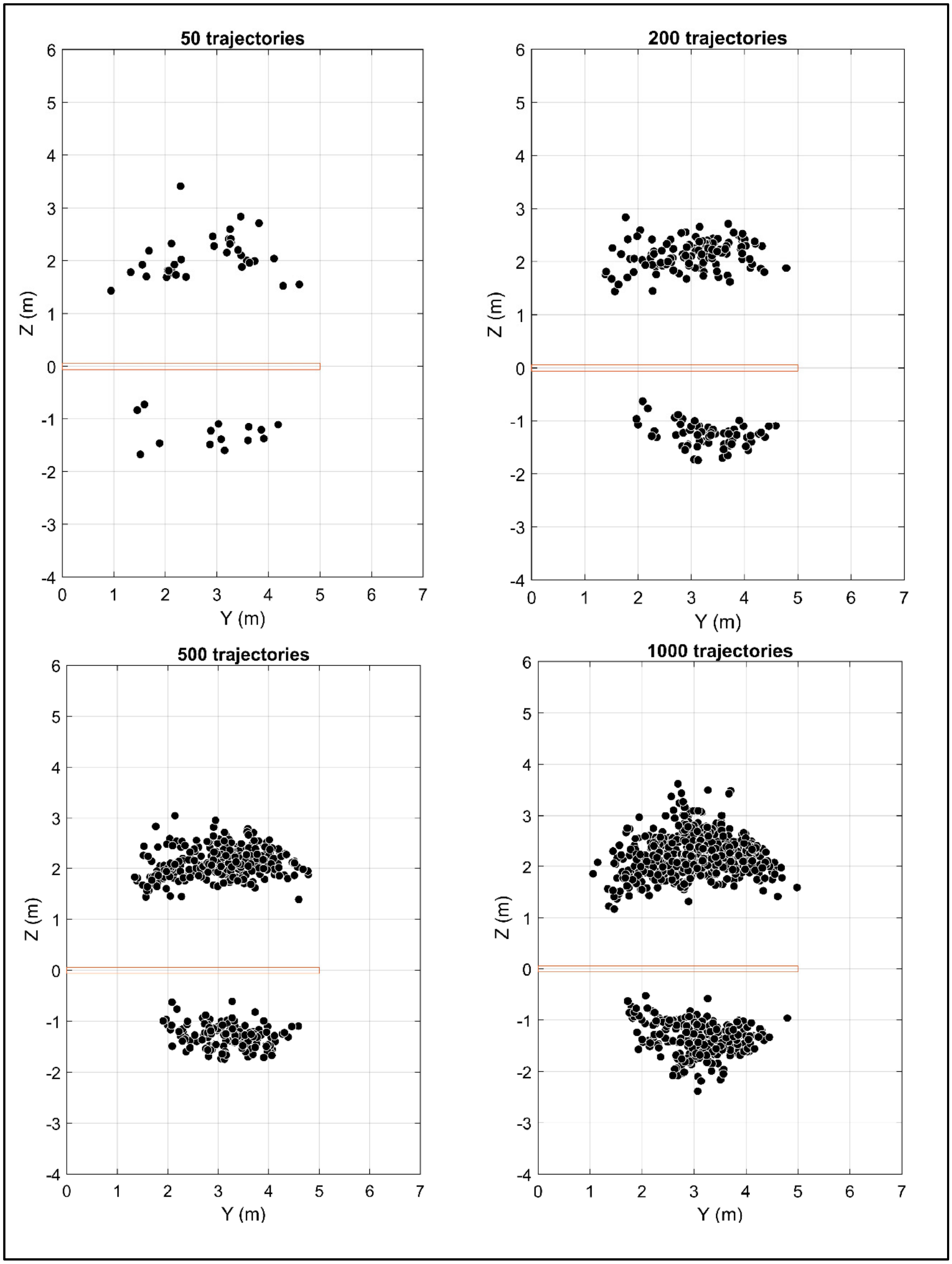

Figure 3.21 Variation of number of trajectories footprint at plan = 6.5 m, AOA = 5°, SBA = 30°.

Figure 3.22 represents the effect of the variation of number of trajectories at the plan of interest downstream the flow. 50, 200, 500, 1000 and 5000 trajectories are simulated. The same procedure done previously for the angle of attack is used for the sweepback angle. To study how the probability distribution of the trajectory's footprints changes with the number of trajectory, a projection of P (Y, Z) is made along the z-axis called P(Z), and along the y-axis called P(Y).

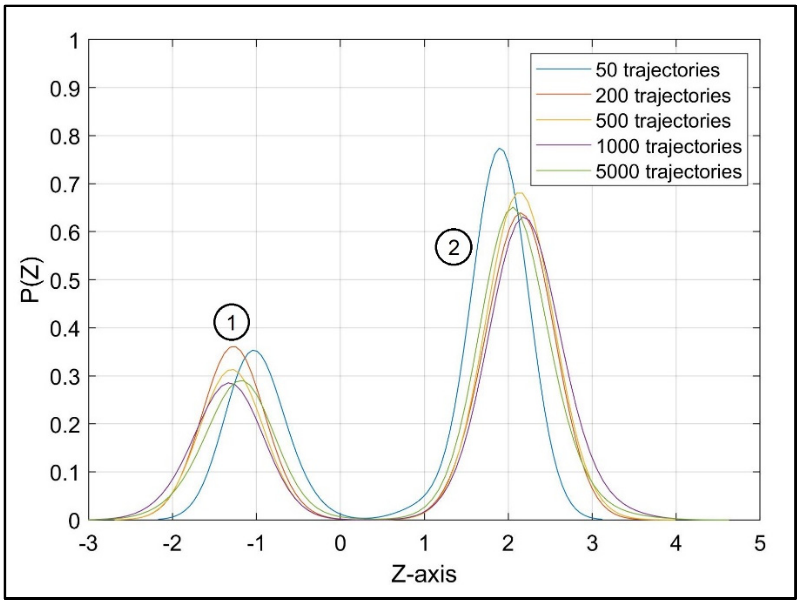

Figure 3.22 Probability distribution of the trajectory's footprint with respect to the z-axis.

Figure 3.22 shows the plotted data P(Z) by means of KSPDF. This function is divided into two subfunctions. The function one is for the negative data which are the footprints downside the wing and function two is for the positive data which are the footprints upside of the wing. After the CDF is plotted, the KS-test is applied for normality with the same procedure done in the angle of attack section.

Figure 3.23 shows the comparison between the empirical CDF (ECDF) and hypothesized CDF (HCDF) for P(Z) for 500 and 1000 trajectories. The set error between the two curves lies on the criteria of the KS test with a maximum error of 5%. After computing the error for the first and second function at 500 trajectories, the maximum error was found 2.74%. The maximum error for the 1000 trajectories was computed to be 2.61% between the ECDF and HCDF.

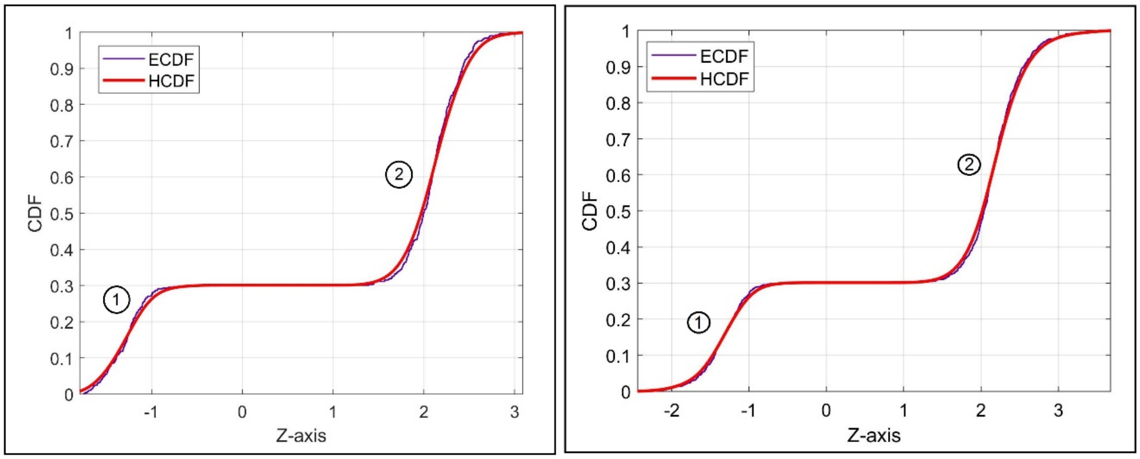

(a)

(b)

Figure 3.23 Cumulative distribution function for 500 (a) and 1000 trajectories (b).

Figure 3.24 shows the means of the projection P(Z) with respect to the number of trajectories. Mean 1 at 50 trajectories was -1.05. The mean decreased at 200 trajectories to attain -1.21, -1.33 at 500 trajectories, 1.342 at 1000 trajectories and 1.321 at 5000 trajectories. At 50 trajectories the mean (2) was around 1.906. When the number of simulated trajectories increases the mean increases until it reaches a value of 2.231 at 500 trajectories 2.235 at 1000 trajectories and 2.241 at 5000 trajectories.

Figure 3.25 shows the variances of the projection P(Z) with respect to the number of trajectories. At 50 trajectories, the variance 1 and variance 2 were at 0.0705 and 0.077 respectively. When the number of simulated trajectories increases both variances decreases until variance 1 and variance 2 reached 0.0485 and 0.071 respectively at 500 trajectories, 0.049 and 0.071 at 1000 trajectories, 0.05 and 0.072 at 5000 trajectories.

The mean and variance variation at 500 and 1000 trajectories are the sign for the probability distribution stabilization. They showed that after 500 trajectories, P(Z) will not change significantly (at an error of 0.01) even after 1000 trajectories and 5000 trajectories. But P(Z) estimation alone is not enough, P(Y) also should comply to the KS-test.

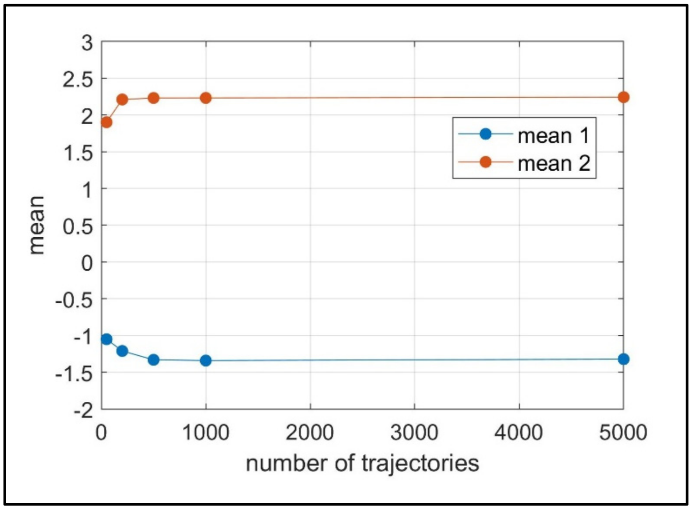

Figure 3.24 Mean variation vs number of trajectories of P(Z), SBA = 30°, AOA=5°.

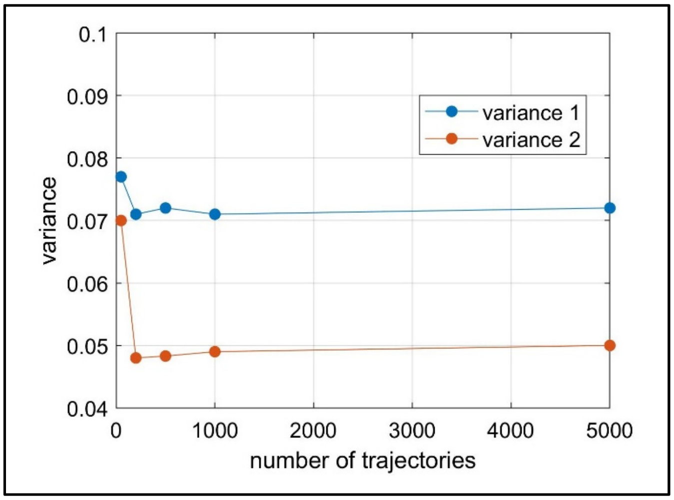

Figure 3.25 Variance variation vs number of trajectories of P(Z), SBA=30°, AOA=5°.

P (Y, Z) is also projected along the Y-axis. This projection is called P(Y). The projection was done for 50, 200, 500,1000 and 5000 trajectories. The P(Y) of the mentioned number of trajectories is illustrated in the Figure 3.26.

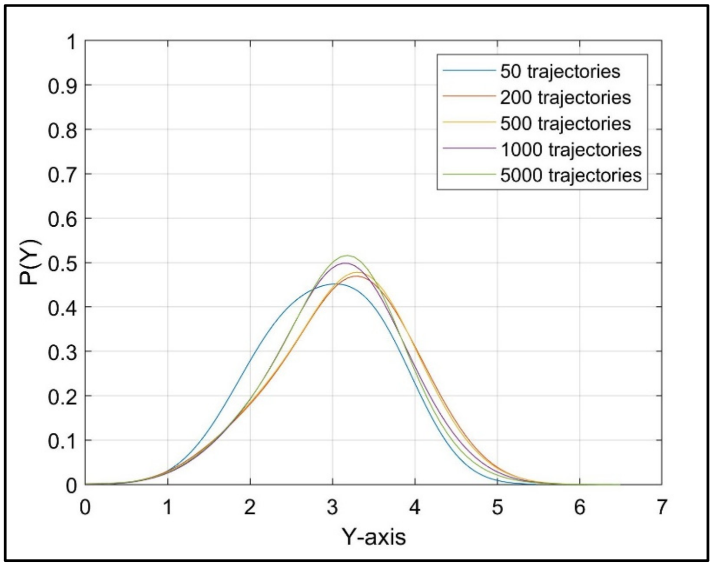

Figure 3.26 Probability distribution of the trajectory's footprint with respect to the y-axis.

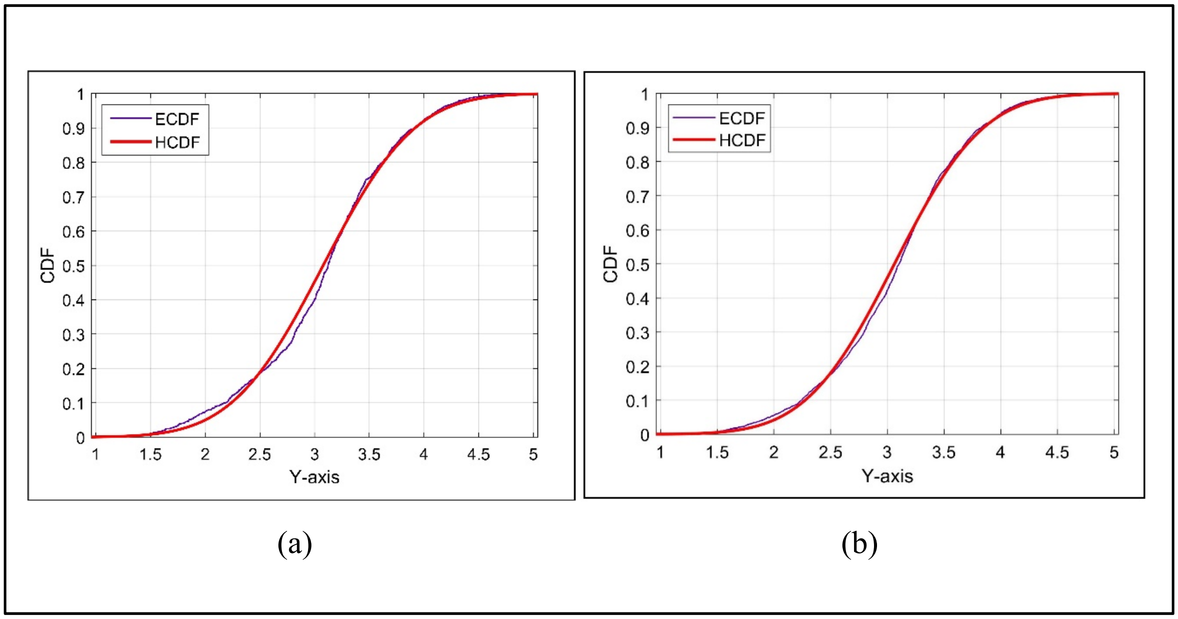

Figure 3.27 Cumulative probability distribution for P(Y) for 500 (a) and 1000 trajectories (b).

Figure 3.27 shows the comparison between the empirical CDF (ECDF) and hypothesized CDF (HCDF) for P(Y). After computing the error for the first and second function at 500 trajectories, the maximum error at y = 2.8 m was found 4.03%. The maximum error computed for the 1000 trajectories is 1.85% between the ECDF and HCDF at y = 3 m .

After proving the normality of P(Y), an estimation of the footprint map should be done. The Monte-Carlo simulation is used to correctly predict this distribution. To fulfill the Monte-Carlo simulation a correct number of trajectories should be simulated. The correct number of trajectories, which should be simulated, is based on the mean and variance of the PDFs. Up to a certain accuracy, the mean and variance of the PDFs shouldn't change. This study will be illustrated in the next two figures.

Figure 3.28 and Figure 3.29 shows the mean and variance distribution respectively of P(Y) with respect to the number of trajectories. In figure 3.29, the mean is 2.901 at 50 trajectories. After the number of simulated trajectories increases the mean increases to reach 3.151 at 500 trajectories, 3.142 at 1000 trajectories and 3.139 at 5000 trajectories. The variance in Figure 3.29 is 0.41 at 50 trajectories. The variance increased with the increased of number of trajectories to reach 0.490 at 500 trajectories, 0.482 at 1000 trajectories and 0.484 at 5000 trajectories.

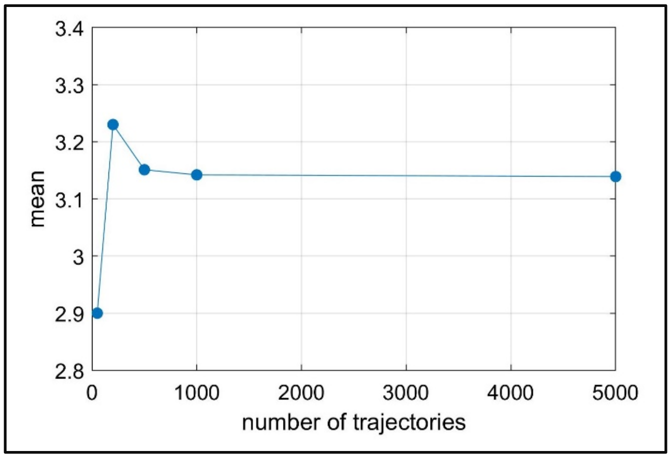

Figure 3.28 Mean variation vs number of trajectories P(Y), SBA=30°, AOA=5°.

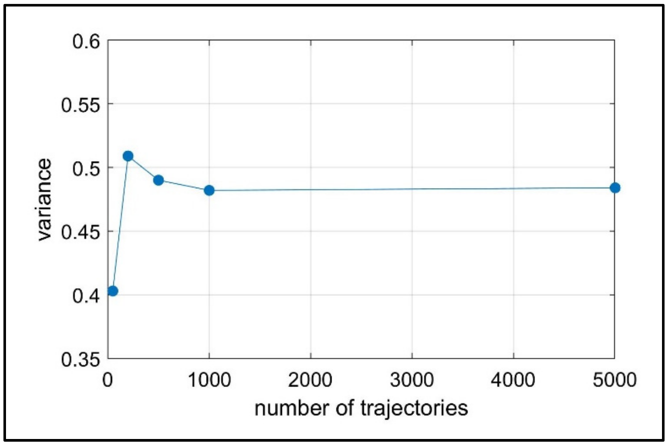

Figure 3.29 Variance variation vs number of trajectories P(Y), SBA=30°, AOA=5°.

Like P(Z) the mean and variance doesn't change significantly at 500 trajectories which indicate the minimal number of simulations needed to fulfill Monte-Carlo method to predict a correct footprint map. As a conclusion, since P(Z) and P(Y) had the stabilization at a precision of 0.01 concerning the mean and the variance. In other words, the difference between the means and the variances of P(Z) and P(Y) at 500, 1000 and 5000 trajectories respectively are less than 0.01.

CONCLUSION

The ice accretion causes degradation of wing lift capability. Such problem could be solved by removing the ice employing some de-icing or anti-icing methods. The removed ice particles fly downstream and can damage the aircraft parts. Statistical and probabilistic studies are done in the literature to compute the area where the ice particles are more likely to pass downstream and to check their possibilities to hit the engine. Experimental and numerical methods are presented to compute the trajectories of the ice particles around a wing. In this research a numerical method is utilized which depicts a footprint map at the engine inlet plane. The footprints are drawn by means of the crossed trajectories. To effectuate this study, a Monte-Carlo method is used. The aim of this research is to build a tool that enables quick study of the wing geometry on footprint maps.

Firstly, a flow field using a 3DPM was used. The 3DPM solver used at the beginning deals with a wing with open wingtip which raises the doubt about the obtained results for verification. Thus, a methodology to close the wing tip was introduced and applied to the 3DPM code solver. The addition of the wing tip corrects the flow around the wing and play an important role in validating the results against the NASA experiments. Secondly, the trajectory code based on CFD solution was available in the literature. However, the trajectory code in this research was adapted to take the flow field solution from the 3DPM code solver instead of taking it from the CFD solution. This integration avoids CFD meshing and eases the task to generate mesh.

A validation of the results against the experiments is conducted as well as verifications with respect to the open source software XFLR5. The probability distribution of the footprints at a plan after the wing was also verified against the results from the literature. After validating and verifying the numerical codes, a parametric study for predicting the footprint map at a plane of the engine was performed. The parametric study involves a probabilistic study by assuming the shape of the PDFs. The footprints are obtained in the (Y, Z) plan thus the probability distribution was obtained in 3D. It is rather complex to predict a correct shape for the 3D PDF by changing the number of trajectories. To avoid this complexity 3D PDF is projected along Y-axis and Z-axis. Therefore, a hypothesis to predict the shape of the PDF was assumed as normal for P(Y) and binormal for P(Z). To validate this hypothesis two test cases was considered: the first case is by fixing the sweepback angle while varying the angle of attack and the number of trajectories, while the second case is by fixing the angle of attack while varying the sweepback angle and the number of trajectories. After calculating the PDFs for every set of trajectories, the PDFs are tested for normality and confirmed using the KS-test. The minimal number of trajectories required to fulfill the Monte-Carlo simulation is estimated. The criteria to estimate the number of trajectories is by comparing the mean and variance for the PDFs linked to the number of trajectories simulated. The criteria to check the minimal number of trajectories was set to a precision between the means and variances of 0.01. It was found that 500 trajectories are capable of estimating a footprint map saving computational time and capabilities.

These results are obtained from a developed MATLAB code for trajectories calculations in 3D. Further works could be done to improve this code. Recommendation for future work could be illustrated as following:

- Take into account the whole aircraft as a geometry, not just a wing to check the effect of the body on the PDFs.
- Work could be used to check the probability of particles that could be ingested by the engine according to the minimal number of trajectories obtained.
- Improving the code to offer more flexibility to define the variable parameters to check its effect on the PDFs for further research.

ANNEX I

VIEW OF THE TRAJECTORIES WITH DIFFERENT SEEPBACK ANGLES AND NUMBER OF TRAJECTORIES

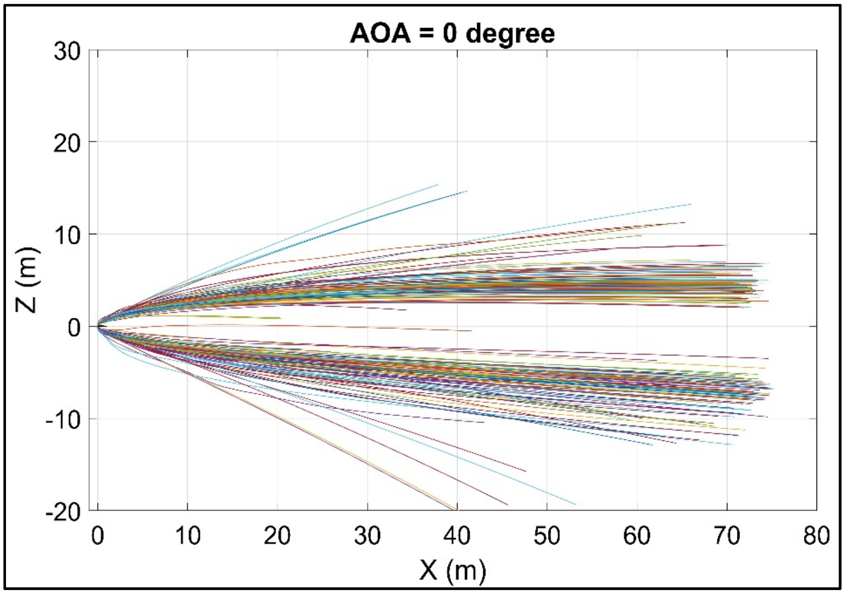

Figure A I-1 XZ view at AOA = 0°.

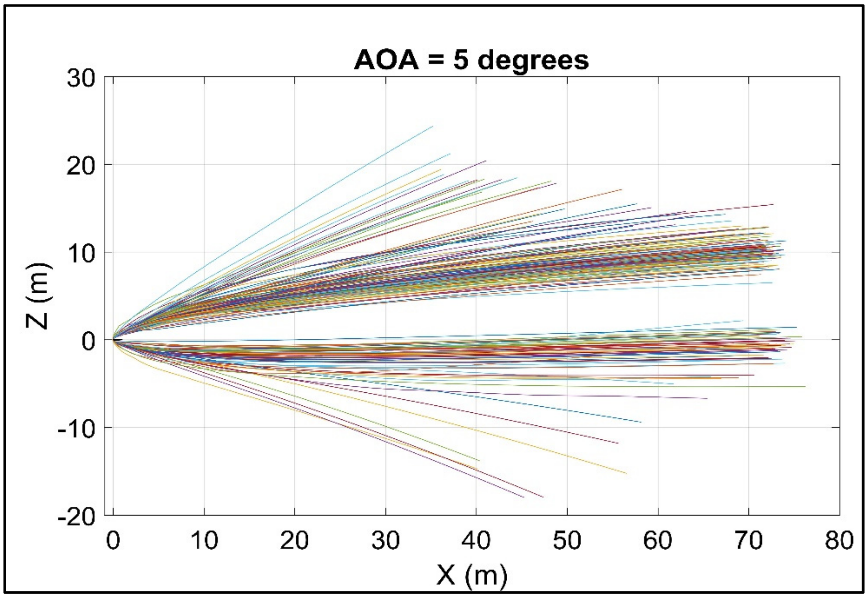

Figure A I-2 XZ view at AOA = 5°.

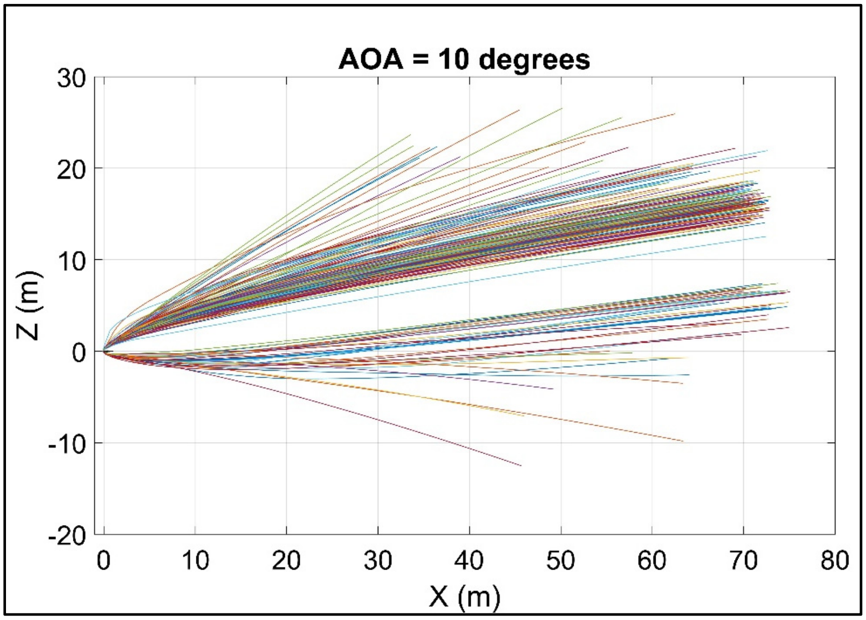

Figure A I-3 XZ view at AOA = 10°.

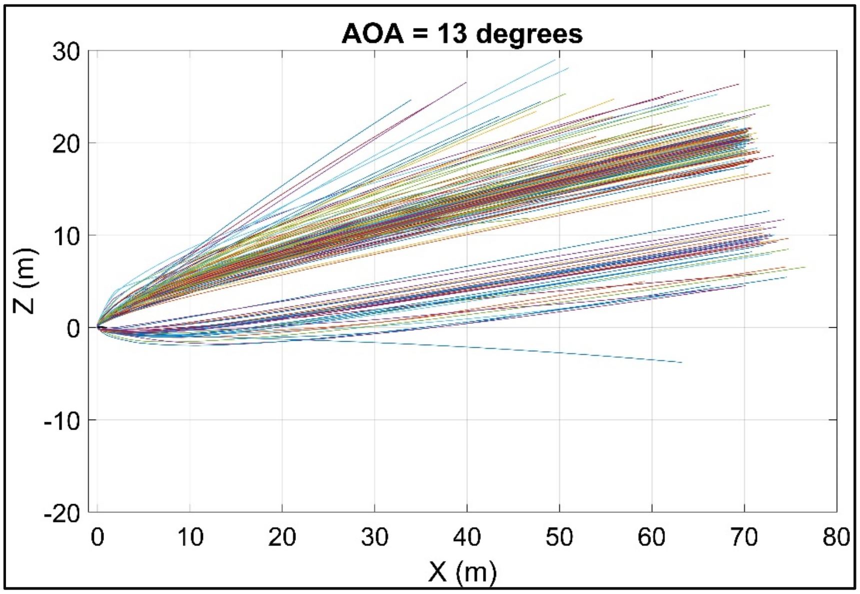

Figure A I-4 XZ view at AOA = 13°.

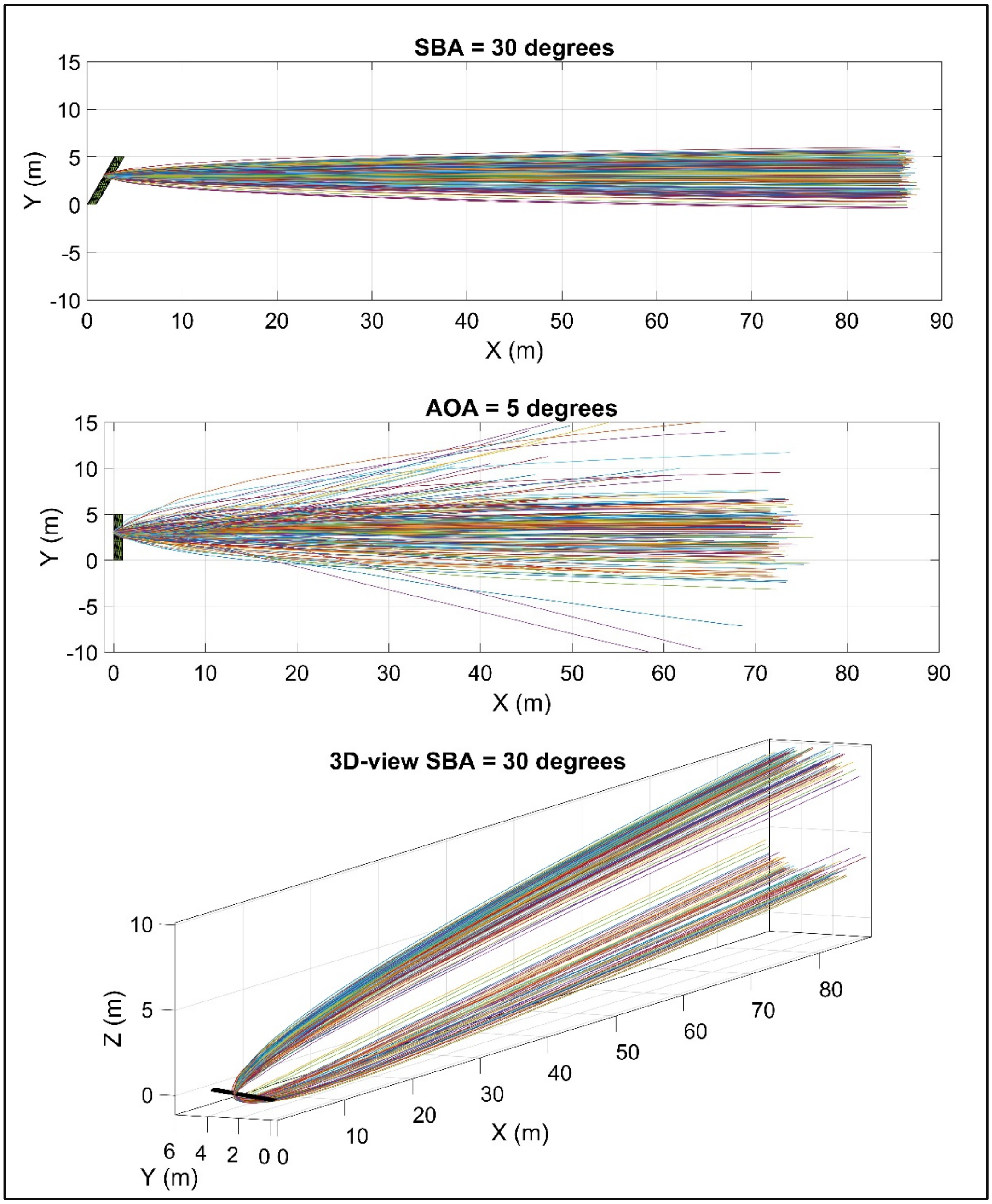

Figure A I-2 Trajectories variation with the varition of SBA.

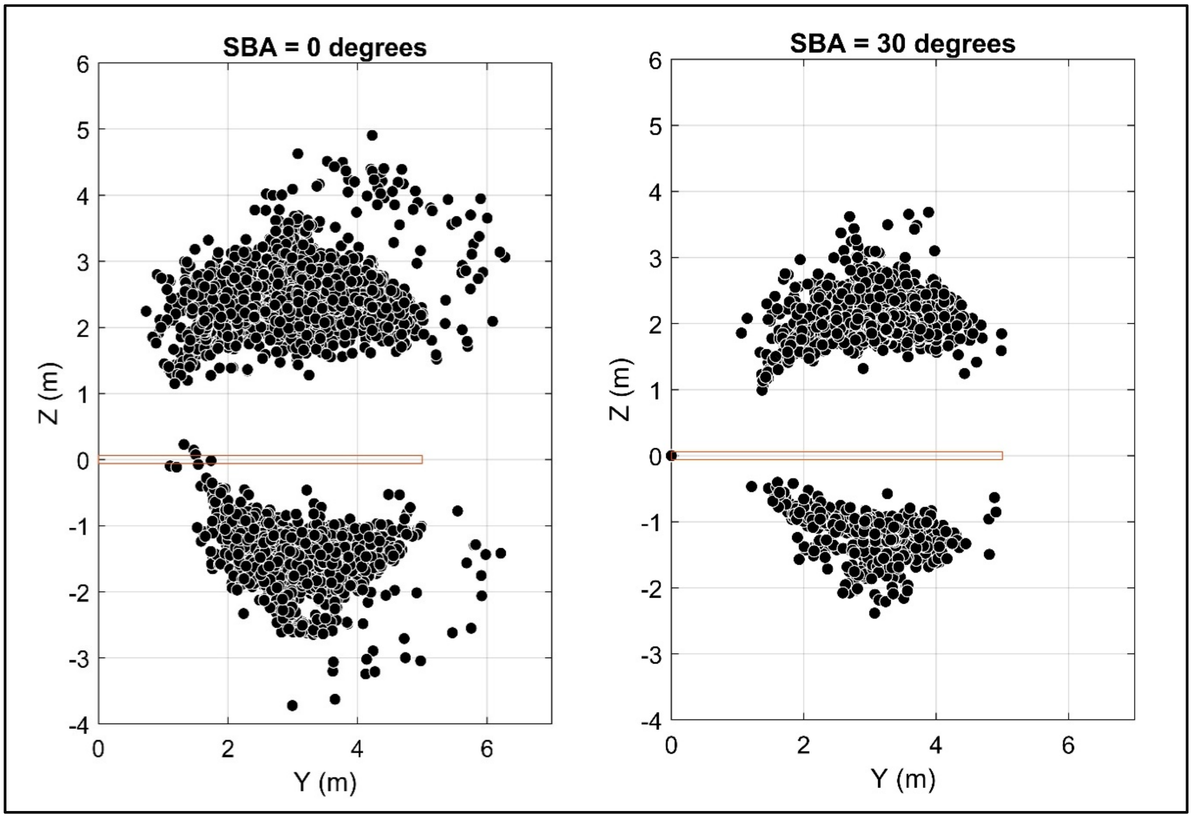

Figure A I-3 5000 trajectories of SBA = 0° and SBA = 30° at AOA= 5°.

LIST OF BIBLIOGRAPHICAL REFERENCES

AOPA. (2008). ASF Safety Advisor on *Aircraft Icing,* with flying tactics for flying in icing conditions. Retrieved from www.aopa.org/asf/publications/sa11.html.

Ashby, D. L., Dudley, M. R., Iguchi, S. K., Browne, L., & Katz, J. (1991). Potential flow theory and operation guide for the panel code PMARC.

Baruzzi, G. S., Lagacé, P., Aubé, M. S., & Habashi, W. G. (2007). *Development of a Shed-ice Trajectory Simulation in FENSAP-ICE*. SAE Technical Paper.

Bowman, A. W., & Azzalini, A. (1997). *Applied smoothing techniques for data analysis: the kernel approach with S-Plus illustrations* (Vol. 18). OUP Oxford.

Cao, Y., Zhang, Q., & Sheridan, J. (2019). *NUMERICAL SIMULATION OF ICE ACCRETION ON AIRFOILS.*

Cebeci, T., & Besnard, E. (1994). Prediction of the performance degradation of an aircraft in natural icing conditions. Dans *32nd Aerospace Sciences Meeting and Exhibit* (pp. 487).

Chandrasekharan, R., & Hinson, M. (2003). *Trajectory simulation of ice shed from a business jet*. SAE Technical Paper.

Deperrois, A. (2009). XFLR5 Analysis of foils and wings operating at low Reynolds numbers. *Guidelines for XFLR5.*

Deschenes, J.-M., Baruzzi, G. S., Lagace, P., & Habashi, W. G. (2011). *FENSAP-ICE: a CFD Monte Carlo approach to shed-ice trajectory and impact*. SAE Technical Paper.

Diebel, J. (2006). Representing attitude: Euler angles, unit quaternions, and rotation vectors. *Matrix, 58*(15-16), 1-35.

Economon, T. D., Palacios, F., Copeland, S. R., Lukaczyk, T. W., & Alonso, J. J. (2015). SU2: An open-source suite for multiphysics simulation and design. *Aiaa Journal, 54*(3), 828-846.

Fu, A. M., Huang, P., & Gu, M. (2013). Numerical model of three-dimensional motion of plate-type wind-borne debris based on quaternions and its improvement in unsteady flow. Dans *Applied Mechanics and Materials* (Vol. 405, pp. 2399-2408). Trans Tech Publ.

Giamati, M. J., Leffel, K., & Wilson, T. M. (1995). Electrical heater de-icer: Google Patents.

Harris, C. D. (1981). Two-dimensional aerodynamic characteristics of the NACA 0012 airfoil in the Langley 8 foot transonic pressure tunnel.

Hess, J. L., & Smith, A. M. O. (1967). Calculation of potential flow about arbitrary bodies. *Progress in Aerospace Sciences, 8*, 1-138.

Holmes, J., Letchford, C. W., & Lin, N. (2006). Investigations of plate-type windborne debris—Part II: Computed trajectories. *Journal of Wind Engineering and Industrial Aerodynamics, 94*(1), 21-39.

Ignatowicz, K., Morency, F., & Lopez, P. (2019). Dynamic Moment Model for Numerical Simulation of a 6-DOF Plate Trajectory around an Aircraft. *Journal of Aerospace Engineering, 32*(5), 04019069.

Katz, J., & Plotkin, A. (2001). *Low-speed aerodynamics* (Vol. 13). Cambridge university press.

Kohlman, D., & Winn, R. (2001). Analytical prediction of trajectories of ice pieces after release in an airstream. Dans *39th Aerospace Sciences Meeting and Exhibit* (pp. 680).

Kordi, B., & Kopp, G. A. (2009). Evaluation of quasi-steady theory applied to windborne flat plates in uniform flow. *Journal of engineering mechanics, 135*(7), 657-668.

Mason, J., Strapp, W., & Chow, P. (2006). The ice particle threat to engines in flight. Dans *44th AIAA Aerospace Sciences Meeting and Exhibit* (pp. 206).

Massey Jr, F. J. (1951). The Kolmogorov-Smirnov test for goodness of fit. *Journal of the American statistical Association, 46*(253), 68-78.

Nassar, M., Guizani, L., Nollet, M.-J., & Tahan, A. (2019). A probability-based reliability assessment approach of seismic base-isolated bridges in cold regions. *Engineering Structures, 197*, 109353.

Papadakis, M., Yeong, H.-W., & Suares, I. (2007). Simulation of ice shedding from a business jet aircraft. Dans *45th AIAA Aerospace Sciences Meeting and Exhibit* (pp. 506).

Papadakis, M., Yeong, H.-W., Wong, S.-C., Vargas, M., & Potapczuk, M. (2005). Experimental investigation of ice accretion effects on a swept wing.

Petrenko, V. F. (2010). System And Method For Icemaker And Aircraft Wing With Combined Electromechanical And Electrothermal Pulse Deicing: Google Patents.

Petty, K. R., & Floyd, C. D. (2004). A statistical review of aviation airframe icing accidents in the US. Dans *Proceedings of the 11th Conference on Aviation, Range, and Aerospace Hyannis*.

Richards, P. J., Williams, N., Laing, B., McCarty, M., & Pond, M. (2008). Numerical calculation of the three-dimensional motion of wind-borne debris. *Journal of Wind Engineering and Industrial Aerodynamics, 96*(10-11), 2188-2202. doi: 10.1016/j.jweia.2008.02.060. Repéré à <Go to ISI>://WOS:000259340500054

Santos, L., Papa, R., & Do Areal Ferrari, M. (2003). *A Simulation Model for Ice Impact Risk Evaluation*. doi: 10.2514/6.2003-30

Shimoi, K. (2010). *Numerical and experimental investigation of ice shedding* (Wichita State University).

Suares, I. G. (2005). *Ice particle trajectory simulation* (Wichita State University).

Tachikawa, M. (1983). Trajectories of flat plates in uniform flow with application to wind-generated missiles. *Journal of Wind Engineering and Industrial Aerodynamics, 14*(1-3), 443-453.

Tagawa, G. d., Morency, F., & Beaugendre, H. (2018). CFD study of airfoil lift reduction caused by ice roughness. Dans *2018 Applied Aerodynamics Conference* (pp. 3010).

Tarafder, M. S., Saha, G. K., & Mehedi, S. T. (2010). Analysis of potential flow around 3-dimensional hydrofoils by combined source and dipole based panel method. *Journal of Marine Science and Technology, 18*(3), 376-384.

Védie, L., Morency, F., & Kubler, N. (2016). Sensitivity analysis of ice piece trajectory calculation. Dans *8th AIAA Atmospheric and Space Environments Conference* (pp. 4351).

Venna, S. V., & Lin, Y.-J. (2006). Mechatronic development of self-actuating in-flight deicing structures. *IEEE/ASME Transactions on mechatronics, 11*(5), 585-592.